TALLINN UNIVERSITY OF TECHNOLOGY
SCHOOL OF ENGINEERING

Department of Materials and Environmental Technology

REACTIVE DIP-COATING OF P-TYPE TRANSPARENT SEMICONDUCTING $CuAlO_2$

P-TÜÜPI LÄBIPAISTVA POOLJUHI $CuAlO_2$ REAKTIIVNE SUKELDUSPINDAMINE

MASTER THESIS

Student	Ali Saffar Shamshirgar
Student code	156327KAYM
Supervisor	Prof. Irina Hussainova Dr. Marina Aghayan

Tallinn, 2017

AUTHOR’S DECLARATION

Hereby I declare, that I have written this thesis independently.
No academic degree has been applied for based on this material.
All works, major viewpoints and data of the other authors used in this thesis have been referenced.

“.......” .... 201…..

Author: Ali Saffar Shamshirgar
/signature /

Thesis is in accordance with terms and requirements

“.......” .... 201….

Supervisor: Irina Hussainova
/signature/

Accepted for defence

“.......”....................201… .

Chairman of theses defence commission: ....
/name and signature/

TALLINNA TEHNIKAÜLIKOOL
INSENERITEADUSKOND

Materjali ja keskkonnatehnoloogia instituut

P-TÜÜPI LÄBIPAISTVA POOLJUHI $CuAlO_2$ REAKTIIVNE SUKELDUSPINDAMINE

REACTIVE DIP-COATING OF P-TYPE TRANSPARENT SEMICONDUCTING $CuAlO_2$

MAGISTRITÖÖ

Üliõpilane:	Ali Saffar Shamshirgar
Üliõpilaskood:	156327KAYM
Juhendaja:	Prof. Irina Hussainova Dr. Marina Aghayan

Tallinn, 2017

AUTORIDEKLARATSIOON

Olen koostanud lõputöö iseseisvalt.
Lõputöö alusel ei ole varem kutse- või teaduskraadi või inseneridiplomit taotletud.Kõik töö koostamisel kasutatud teiste autorite tööd, olulised seisukohad, kirjandusallikatest ja mujalt pärinevad andmed on viidatud.

“.......” .... 201…..

Autor: Ali Saffar Shamshirgar
/ allkiri /

Töö vastab bakalaureusetöö/magistritööle esitatud nõuetele

“.......” .... 201…..

Juhendaja: Irina Hussainova
/ allkiri /

Kaitsmisele lubatud

“.......”....................201… .

Kaitsmiskomisjoni esimees ....
/ nimi ja allkiri /

CONTENTS

CONTENTS 4
ABBREVIATIONS AND ACRONYMS 6
1. INTRODUCTION 7
2. REVIEW OF THE LITERATURE 9
  2.1 Semiconductors 9
  2.2 p-n Junctions 10
  2.3 Transparent Oxide Semiconductors 14
  2.4 Light-Matter Interaction 15
    2.4.1 Absorption 15
    2.4.2 Reflection and Transmission 16
    2.4.3 Transparency/Translucency 18
  2.5 Properties and applications of alumina nanofibers 20
  2.6 Characteristics of the final product 22
    2.6.1 Delafossite Copper Aluminate 22
    2.6.2 Spinel Copper Aluminate 23
  2.7 Pulsed Laser Deposition [PLD] 25
  2.8 Objectives 26
3. EXPERIMENTAL AND CHARACTRIZATION 27
  3.1 Bulk Preparation 27
    3.1.1 Synthesis 27
    3.1.2 Consolidation and Sample Preparation 29
    3.1.3 Ball Milling 29
  3.2 Thin Film Deposition 30
    3.2.1 Target Preparation 30
    3.2.2 Deposition Mechanism 30
  3.3 Characterization Techniques 30
    3.3.1 X-ray Diffraction 30
    3.3.2 Scanning Electron Microscopy 31
    3.3.3 Thermal Analysis 32
    3.3.4 Resistivity Measurement 32
    3.3.5 UV-Visible Spectroscopy 33

3.3.6 Thermoelectric Power Measurement 34
3.3.7 Hall Effect Measurement 34
4 RESULTS AND DISCUSSION 35
4.1 Microstructure and Crystal Structure 35
4.2 Thermodynamics of the process 40
4.3 Electrical Conductivity 41
4.4 Optical Properties 42
4.5 Thermoelectric Power 43
4.6 Hall measurement 45
5. CONCLUSIONS 47
6. Résumé 48
7. Resümee 49
8. REFERENCES. 50
9. ACKNOWLEDGEMENTS 54

ABBREVIATIONS AND ACRONYMS

UV - Ultra Violet

ANF - Alumina Nano-Fiber

TCO - Transparent Conductive Oxide

TOS - Transparent Oxide Semiconductor

EDS - Energy Dispersive Spectroscopy

1D – One-Dimensional

TGA - Thermogravimetric Analysis

DTA - Differential Thermal Analysis

SEM - Scanning Electron Microscope

TEM - Transmission Electron Microscope

TM - Transition Metal

XRD - X-ray Diffraction

wt.% - Weight percentage

SCS - Solution Combustion Synthesis

SHS - Self-propagating High temperature Synthesis

VCS - Volume Combustion Synthesis

UV-Vis - Ultra Violet-Visible light spectroscopy

TGA - Thermogravimetry Analysis

DTA - Differential Thermal Analysis

DSC - Differential Scanning Calorimetry

PLD - Pulsed Laser Deposition

1. INTRODUCTION

In transparent electronics, the contradictory approach of having optical transparency together with electronic conduction is the main challenge. The reason behind this challenge is that the prerequisite of optical transparency in materials is having no interaction with photons of visible light portion of electromagnetic spectrum. Meanwhile, electronic conduction demands for smaller energy band gaps so that charge carriers can be excited easier to contribute to optoelectronic current generation. Generally, to absorb UV range of light wavelengths and transmit the visible light photons, energy band gaps larger than 3.1 eV is required [1][2]. To maintain this requirement, transparent conductive oxides [TCOs] are among the best candidates. The first TCO, In_2O_3:Sn (ITO) was reported by Rupperecht [3] in 1954, followed by other TCOs: SnO_2 and ZnO. These materials are known as n-type transparent oxide semiconductors [TOS] and are commercialized for applications in transparent window electrodes and interconnections. The conduction band minimum (CBM) of most metal oxides is made of spatially spread spherical metal *s* orbital. Therefore, electrons in the metal oxides have small effective mass, and high electronic conduction is possible if high-density electron doping is achieved. This is the reason why several n-type TOSs are found to date. In contrast, the valence band maximum (VBM) is made of oxygen 2p orbitals, which are rather localized, leading to small hole effective masses. Furthermore, the dispersion of the valence bands tends to be small, and thus the VBM level is so deep that hole doping is difficult. Therefore, p-type TOS was not discovered before 1997 [2]. The breakthrough was finding of the first p-type TCO, $CuAlO_2$ by Kawazoe et al. [1]. Later, several transparent p-type semiconductors were developed and used in p-n junctions. Nevertheless, the delafossite $CuAlO_2$ still is attracting many interests because of its unique properties. Its structure has extensively studied by Ishiguro et al. [4] and its significance for application in transparent p-n junctions is emphasized. $CuAlO_2$ has a layered crystal structure with Cu atoms between AlO_2 layers forming O–Cu–O pillars [5].

To date, researchers reported various synthesis methods for direct copper aluminate thin film growth and influence of these methods on the final product. Gong et al. [6] succeeded in preparing copper–aluminum oxide films by a chemical-vapor deposition technique with copper acetylacetonate and aluminum acetylacetonate precursors. Tonooka et al. [7] reported solution method in which a solution of copper nitrate and aluminum nitrate was used to make thin film of $CuAlO_2$ directly by spin-drawing. Li et al. [8] prepared $CuAlO_2$ thin films on quartz glass and sapphire substrates by chemical solution deposition method using copper acetate monohydrate, aluminum nitrate nanohydrate and 2-methoxyethanol as starting precursor and solvent.

Approaches for bulk preparation of $CuAlO_2$ are typically based on firing a stoichiometric mixture of Al_2O_3 and CuO/Cu_2O at 1100 °C in air for several hours in multi stage procedures. Zhao et al. [9] obtained fibers of $CuAlO_2$ after the hybrid fibrous mats were thermally treated at 1100 °C in a multi stage electrospinning procedure. Nanostructured $CuAlO_2$ was synthesized by using boehmite (γ-AlOOH) nanorods loaded with Cu(II) acetate as a nanoprecursor at 1150 °C in air in a multi stage procedure [10]. Ahmed et al. [11] reported the synthesis of pure phase 35 nm diameter $CuAlO_2$ nanoparticles at 775 °C under a controlled oxygen partial pressure (pO_2) and at 800 °C under flowing N_2 atmospheres for 48 hours.

Considering that the most synthesis approaches reported, require complex instrumentation, templating, process, or significant amount of time, the scalable and cost-effective production of $CuAlO_2$ is still a challenge. The synthesis of delafossite copper aluminate using the network of alumina nanofibers in a single stage, straightforward, and scalable approach is the main task of this work. The idea is initiated from the fact that nonporous structure of alumina nanofibers would make the heat dissipation within their matrix more efficient. Moreover, a combination of sol-gel and dip-coating can expedite homogenization of the reactive dopants. The phase purity and the morphology of the final product is studied by x-ray diffraction (XRD) and scanning electron microscopy (SEM). Furthermore, electrical, optical, and thermoelectric properties of the synthesized material are thoroughly studied and thermal analysis was considered to explore the thermodynamics of the process. Moreover, possibility of using the final bulk $CuAlO_2$ as target for deposition of thin film using pulsed laser deposition [PLD] technique as a part of the future work of this study is presented in this thesis.

2. REVIEW OF THE LITERATURE

2.1 Semiconductors

Based on their electrical conductivity, materials can be classified in four different categories. While insulators, semiconductors, and conductors with different room temperature resistivity make the first three categories, superconductors are the forth category with no electrical resistivity (Figure 1).

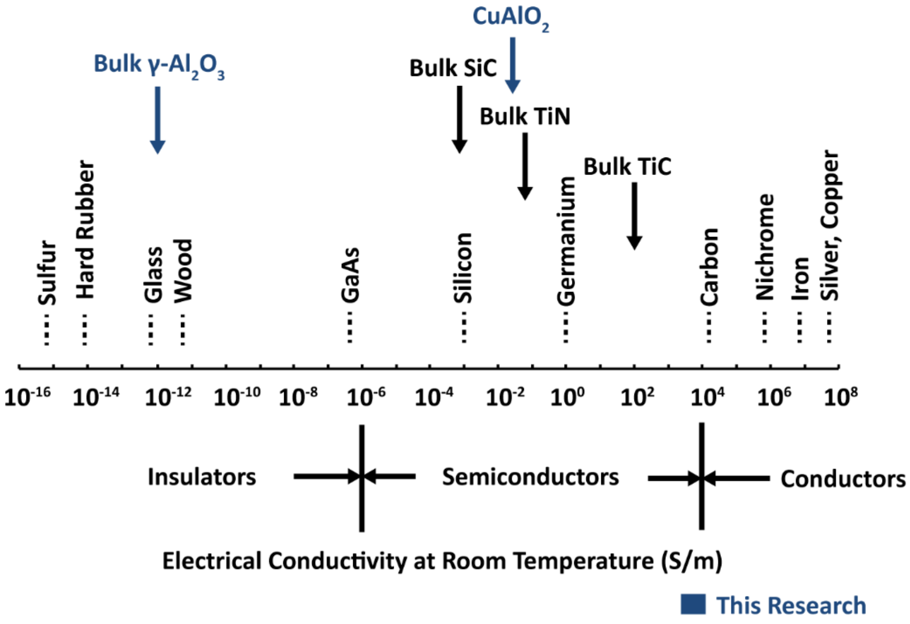

Figure 1: Electrical Conductivity Scale of Materials

The term semiconducting property can be differentiated into two separate subcategories called intrinsic and extrinsic semiconductors. Intrinsic semiconductor is referred to pure undoped material with equal probability for finding electrons in conduction band edge as there is of finding holes at the valence band edge. This equal probability infers the equal number of electrons and holes which implies that Fermi energy level in this type of semiconductor which also is called i-type must lie at the center of forbidden energy gap.

On the contrary, extrinsic semiconductors are those which impurities are introduced to them in order to make charge carriers of a certain species dominant. For n-type semiconductor, there are more electrons in the conduction band than there are holes in the valence band. This also implies that the probability of finding an electron near the conduction band edge is larger than the probability of finding a hole at the valence band edge. Therefore, the Fermi level is closer to the conduction band. In contrast, for p-type semiconductors there are more holes in the valence band than there are electrons in the conduction band. This also implies that the probability of finding an electron near the conduction band edge is smaller than the probability of finding a hole at the valence band edge. Therefore, the Fermi level is closer to the valence band. [12] [13] The Fermi-Dirac distribution function in Figure 2 illustrates the possible energy states for existence of electrons in semiconductors of every type. This figure demonstrates graphs for non-absolute-zero temperature.

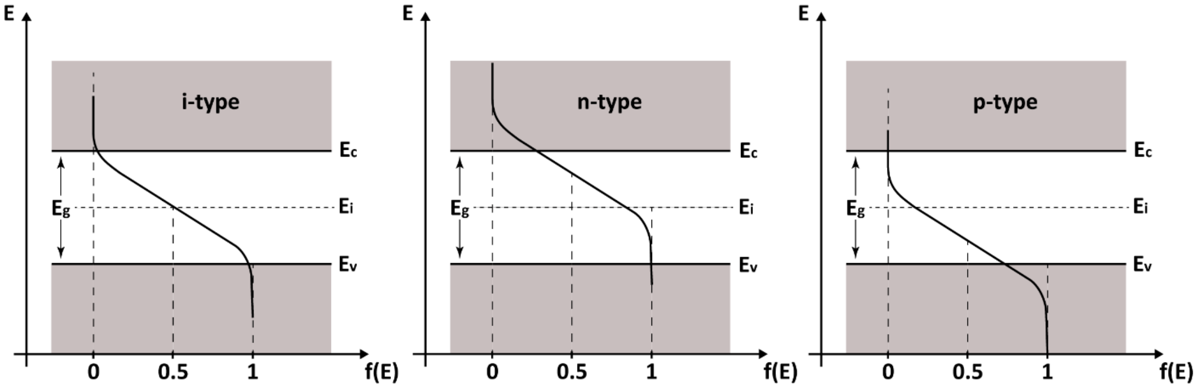

Figure 2: Fermi-Dirac distribution in different semiconductors. Ec: Conduction Band, Ev: Valance Band, Ei: Intrinsic Fermi Level, Eg: Energy Band Gap.

2.2 p-n Junctions

p-n junctions are elementary "building blocks" of electronic devices in the forms of diodes, transistors, LEDs, and integrated circuits; they are the active sites where the electronic action of the device takes place. A p-n junction is a boundary or interface between two types of semiconductor material; p-type and n-type. There are several structural layouts for p-n junctions, each act in a certain way for a specific purpose. When p-type and n-type material are placed in contact with each other, the junction’s response to external excitation is very different than either type of material alone. Specifically, current will flow readily in one direction (forward biased) but the junction blocks the current flow in the other direction (reverse biased), creating the basic diode. This non-reversing behavior arises from the nature of the charge transport process in the two types of materials. When a p-n junction is formed, some of the free electrons in the n-region diffuse across the junction and combine with holes. In so doing they leave behind positive ions at the donor impurity sites. Within this region which is called depletion zone (Figure 3), there are very few mobile electrons and holes. It is "depleted" of mobile charges, leaving only the fixed charges associated with the dopant atoms/molecules. As a result, the depletion region is highly resistive and now behaves as a wall which blocks further diffusion of the charge carriers through one another with Coulomb force.

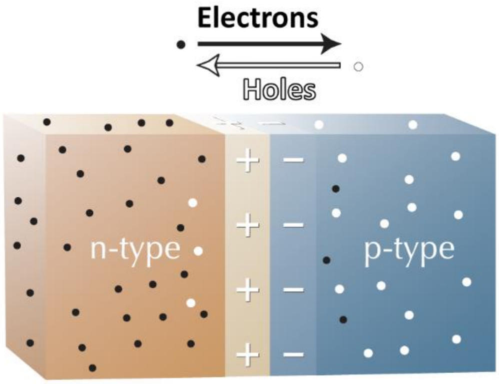

Figure 3: Depletion Region in p-n Junctions

To pass this wall, charge carriers need to be excited with outer sources such as applied electric current. In other words, the resistance of the depletion region can be modified by excitation of an external electric field to the built-in electric field. If the excitation electric field is in the same direction as the built-in electric field, the depletion region's resistance will become greater. If the excitation electric field is opposite in direction to the built-in electric field, the depletion region's resistance will become smaller. The depletion region can therefore be considered to operate as a voltage-controlled resistor. If a positive voltage is applied to the p-type side and a negative voltage to the n-type side, current can flow (depending upon the magnitude of the applied voltage). This configuration is called "Forward Biased" (Figure 4). At the p-n junction, the "built-in" electric field and the applied electric field are in opposite directions. When these two fields add, the resultant field at the junction is smaller in magnitude than the magnitude of the original "built-in" electric field. This results in a thinner, less resistive depletion region. If the applied voltage is large enough, the depletion region's resistance becomes negligible. If a negative voltage is applied to the p-type side and a positive voltage to the n-type side, no (or exceptionally small) current flows. This configuration is called "Reverse Biased" (Figure 6).

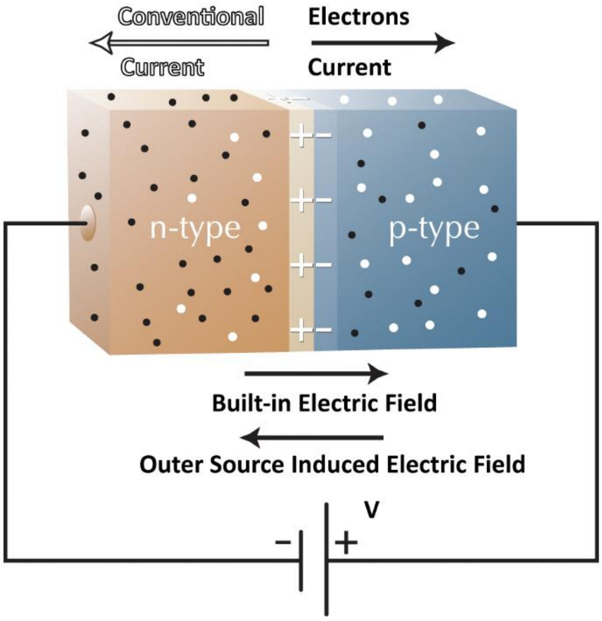

Figure 4: Forward Bias of the p-n Junction

At the p-n junction, the "built-in" electric field and the applied electric field are in the same direction. When these two fields add, the resultant larger electric field is in the same direction as the "built in" electric field and this creates a thicker, more resistive depletion region. If the applied voltage becomes larger, the depletion region becomes thicker and more resistive. In reality, some current will still flow through this resistance, but the resistance is so high that the current may be considered to be zero. As the applied reverse bias voltage becomes larger, the current flow will saturate at a constant but very small value. This is approximately 10-12 A/cm^2 of p-n junction area.

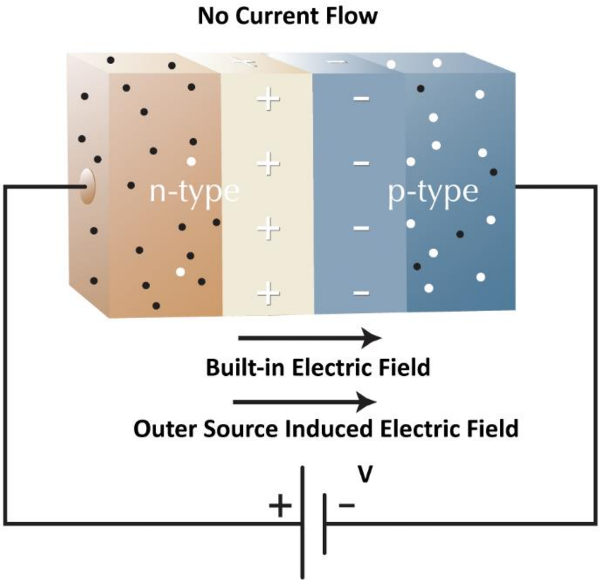

Figure 5: Reverse Bias of the p-n Junction

The current-voltage relation or IV curve of a silicon p-n junction is shown in Figure 6. In reverse bias, the p-n junction exhibits extreme electrical resistance and only a very small current flow. If the reverse bias voltage becomes too large, then the junction will breakdown and current will flow. It is possible to design p-n junctions with selected breakdown voltage at a specific desired threshold. Such p-n junctions are called Zener diodes and are used as voltage references or overvoltage protectors in electrical circuit. In forward bias, the p-n junction exhibits an exponential lowering of resistance with applied voltage. As it is demonstrated in the Figure 6 the junction is extremely resistive when the voltage is having values lower than the exponential region threshold. When the applied voltage approaches the threshold, the exponential nature of the junction causes the resistance to drop dramatically. The p-n junction diode appears to be an electrical switch that "turns on" when the threshold voltage is applied in the forward bias. Because electrical current flows only when it is forward biased, the diode appears to be an electrical one-way valve [14]. On the other hand, in reverse bias the voltage threshold for breakdown is the operational function that Zener diodes undergo.

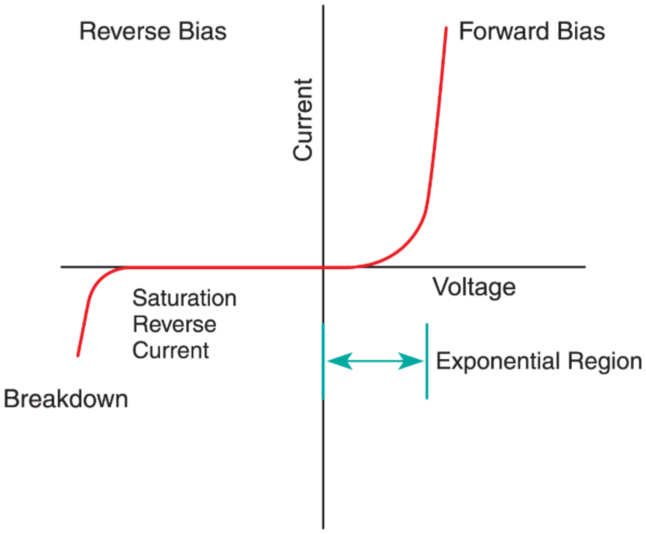

Figure 6: IV curve of the Silicon p-n Junction Diode

2.3 Transparent Oxide Semiconductors

One of the major properties that determines how transparent or translucent a material can be is its optical energy band gap. As it is illustrated in Figure 7 the human eyes can detect a tiny portion of incoming wavelengths (390-700 nm) from the electromagnetic radiations. This range is called visible spectrum. For transparent/translucent material, the energies of the photons from visible range fall into their optical energy band gap or so called forbidden energy gap. This region is the gap between valance band and conductive band where no electron can exist. Therefore, photons of the visible spectrum cannot excite electrons since they do not have enough energy to make electrons jump over the forbidden energy gap. In other words, photons of the visible electromagnetic spectrum do not interact with electrons and can be transmitted. The morphology of the material and its crystalline structure later defines whether it’s going to transmit photons intact or with diffraction which correspond to transparency and translucency terminologies respectively. It is generally believed that high optical transparency is incompatible with high electronic conduction, since optical transparency requires band gaps larger than 3.1 eV and such a large gap makes carrier doping very difficult. In this sense, transparent conductive oxides (TCOs) are exceptional materials.

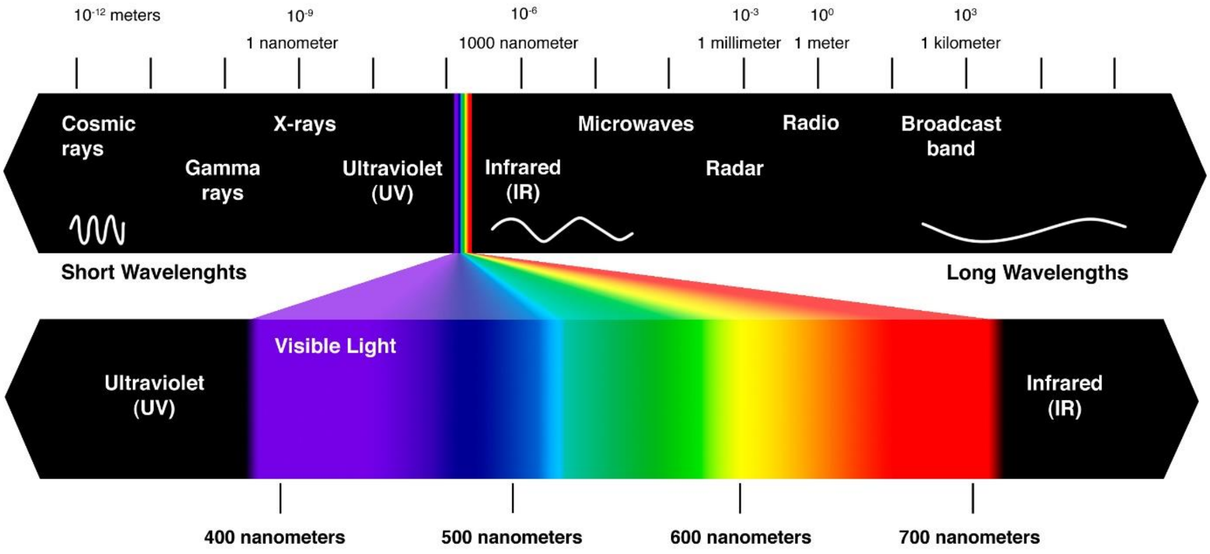

Figure 7: Electromagnetic Spectrum

2.4 Light-Matter Interaction

In classical electrodynamics, light is considered as electromagnetic wave. When incident light wave encounters matter, it either can induce electrons in the matter to change their orbits or not. In case the electronic transition in molecules or atoms (quantum leap) does not occur, wavelength of the incident light is not subject to change. Therefore, the light is reflected, scattered, or transmitted with the original wavelength (λ_1) (Figure 8) (Thickness effect and internal interactions are neglected). If the incoming light incident interact with electrons, causing them to jump to higher orbits, the wavelength of the emitted light which is a result of returning the electrons to their initial state (photoluminescence) would have larger wavelength (λ_2) than the original. [15] However, in reality mostly matter reflects a portion of incoming light from its surface. This reflection together with emitted light and the phenomenon of change in the reflected or emitted light wavelength is the beginning of colors appearance.

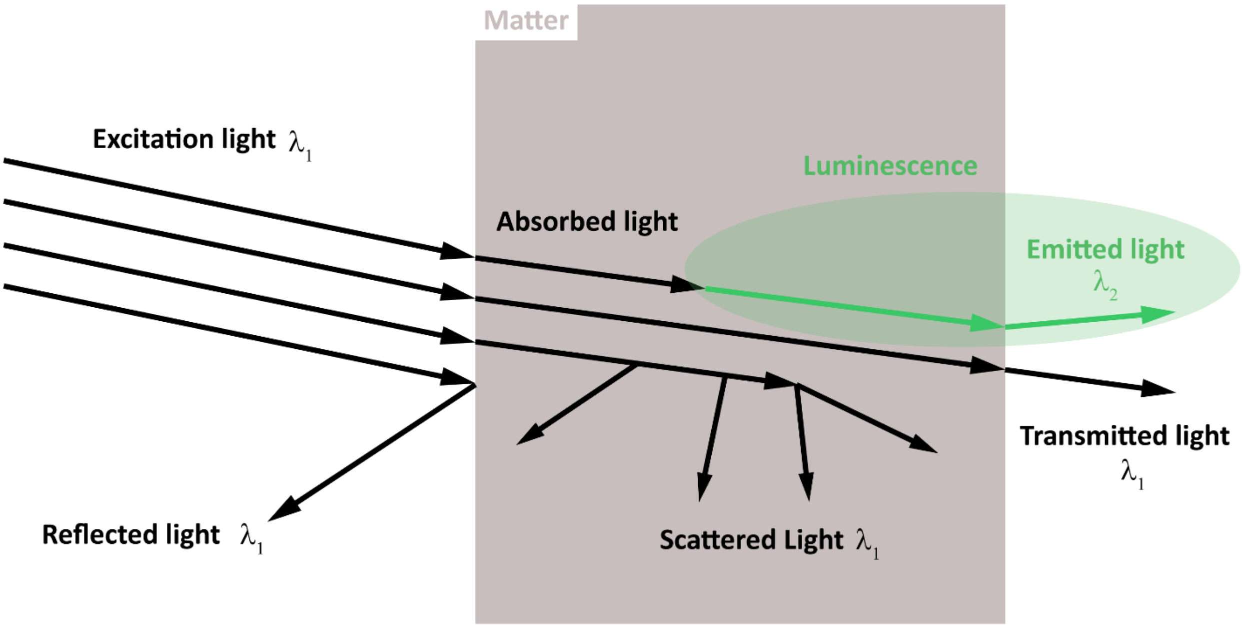

Figure 8: Light-Matter Interaction Phenomena

2.4.1 Absorption

Absorption occurs when the incoming photons cannot pass through the material due to different factors. In metals, photons can cause free electrons of the metallic bond to vibrate if the incoming frequencies are synced with electrons natural vibrational frequencies. This causes vibrational motion in electrons, and consequently makes them interact with neighboring atoms in such a manner as to convert their vibrational energy into thermal energy. Since different atoms of metals have different natural frequencies of vibration, they will selectively absorb different frequencies of visible light. Moreover, the delocalization effect of the "sea of electrons" in metals makes them reflect most of the incoming light. This gives them their metallic color. Most insulators (or dielectric materials) are held together by ionic bonds. Thus, these materials do not have free conduction electrons, and the bonding electrons reflect only a small fraction of the incident wave.

2.4.2 Reflection and Transmission

In general, most light reflection initiates from surface of the material. If surface roughness is low enough to deal with incoming light in a mirror-like manner, the reflection mechanism is called specular or mirror-like reflection. Matter exhibiting this property, retains energy and image (the angle at which the wave is incident on the surface equals the angle at which it is reflected). (Figure 10).

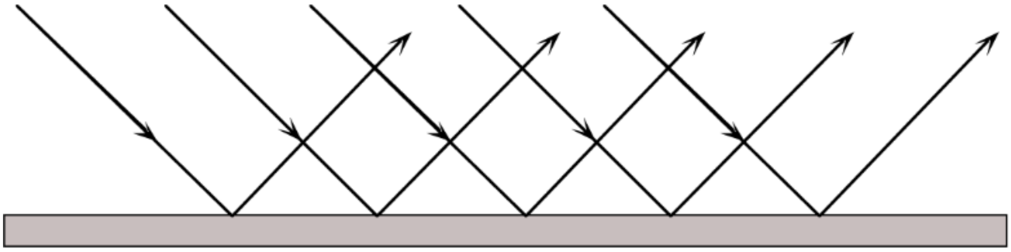

Figure 9: Specular Reflection

If the surface roughness is high, the light is being refracted when bouncing back from the surface in several different angles. This type of reflection is called diffuse reflection. Matter exhibiting this property retains the energy but loses the image (the incident angle is different than reflected angle) (Figure 9). In atomic and molecular structure reflection, light wave incident induces small oscillations of polarization in the individual atoms (or oscillation of electrons, in metals), causing each particle to radiate a small secondary wave in all directions. All these waves add up to give specular reflection and refraction. In the case of dielectrics such as glass, the electric field of the light acts on the electrons in the material, and the moving electrons generate fields and become new radiators. The refracted light in the glass is the combination of the forward radiation of the electrons and the incident light. The reflected light is the combination of the backward radiation of all of the electrons. In metals, when free electrons oscillate with the incident light, the phase difference between their radiation field and the incident field is π (180°), so the forward radiation cancels the incident light, and backward radiation is just the reflected light. [16][17][18]

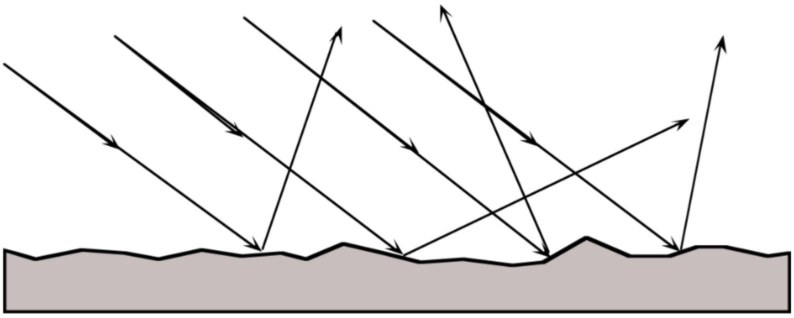

Figure 10: Diffuse Reflection

If a dielectric material does not include light-absorbent additive molecules (pigments, dyes, colorants), it is usually transparent to the spectrum of visible light. Color centers (or dye molecules, or "dopants") in a dielectric absorb a portion of the incoming light. The remaining frequencies (or wavelengths) are free to be reflected or transmitted. This is how colored glass is produced. Most liquids and aqueous solutions are highly transparent. For example, water, cooking oil, rubbing alcohol, air, and natural gas are all clear. Absence of structural defects (voids, cracks, etc.) and molecular structure of most liquids are chiefly responsible for their excellent optical transmission. The ability of liquids to "heal" internal defects via viscous flow is one of the reasons why some fibrous materials (e.g., paper or fabric) increase their apparent transparency when wetted. The liquid fills up numerous voids making the material more structurally homogeneous. Light transmission will be highly directional due to the typical anisotropy of crystalline substances, which includes their symmetry group and Bravais lattice. For example, the seven different crystalline forms of quartz silica (silicon dioxide, SiO2) are all clear, transparent materials. In semiconductors, when the energy of the incoming photon is high enough to make an electron to jump to higher orbits, the incoming quantum of light (or photon) is being absorbed. On the contrary, photons with wavelengths larger than energy band gap of the material are free to be transmitted.

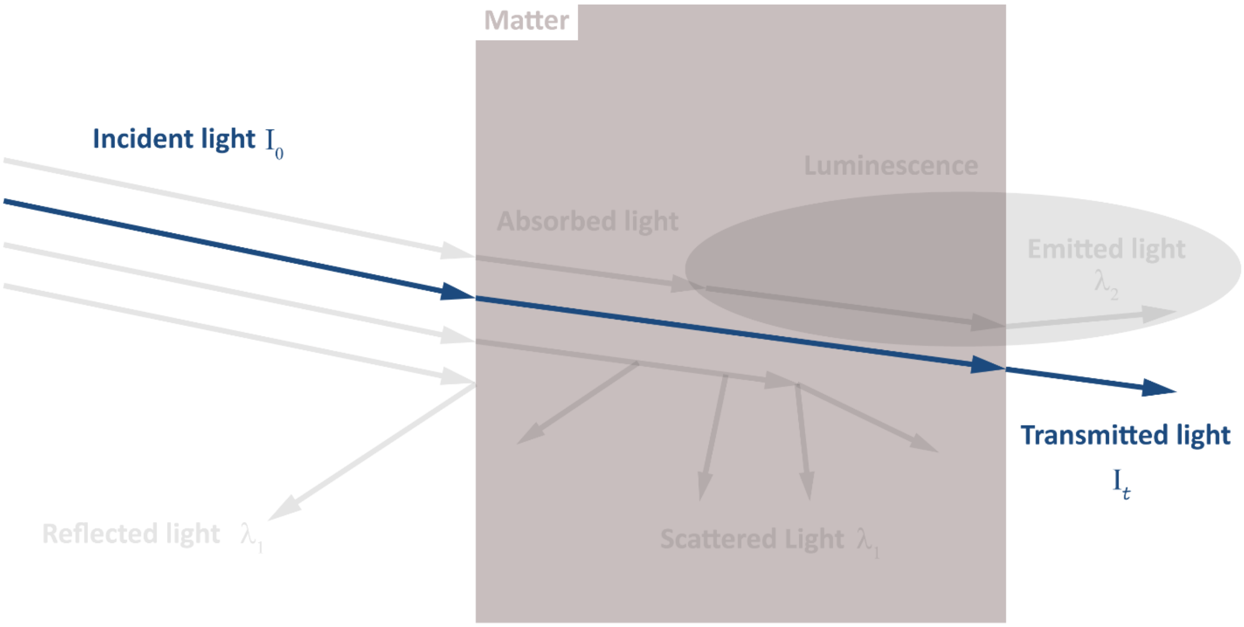

Figure 11: Electromagnetic Wave Transmittance in Matter

To quantify the ability of material to transmit the incoming light, their transmittance can be simply formulated by dividing the transmitted intensities by incident intensities. Equation 1 and Figure 11 demonstrate this correlation.

$$T = \frac{I_t}{I_0} \qquad 0 \leq T \leq 1$$

Equation 1: Transmittance T, Incident intensity I_0, Transmitted intensity I_t

Absorbance can be determined from the Beer-Lambert Law (Equation 2). In this equation, molar extinction coefficient ε has unit of L mol^{-1}cm^{-1}, l is the path length of the sample in cm, and c is the concentration of the compound, expressed in mol L^{-1}.

$$\log\frac{1}{T} = \epsilon c l = A$$

Equation 2: Absorbance A, Transmittance T, molar extinction coefficient ε, length l

2.4.3 Transparency/Translucency

Transmitted light through material consists of the directly transmitted and the diffused components. Depending on the angular distribution of the diffused portion, transparency and translucency can be differentiated. Two mechanisms of narrow angle and wide angle scattering correspond to transparent and translucent nature of the material respectively (Figure 12). Transparency is the property of some materials that allows light to be partially (visible portion of the electromagnetic spectrum) transmitted through. The proportion of light a material transmits through determines its transmittance described in section 2.4.2. The term translucency is generally used in cases where light is diffusely transmitted through. In fact, translucent materials are the exact opposite of opaque materials in the way they respond to incident light. An object may not be transparent either because it reflects the incoming light or because it absorbs the incoming light. Almost all solids reflect a part and absorb a part of the incoming light. The microstructural mechanism which decreases translucency and transparency is existence of scattering centers in the material. In polycrystalline structures, mainly microstructural defects such as pores and grain boundaries are responsible for light scattering. However, impurities and voids can also scatter the incoming incident of light. This effect is minimized in single crystal structures where grain boundaries do not exist and the inefficiency would be mainly due to existence of defects and impurities. In polycrystalline structures, size of the constituent particles of grains is in relation with size of the grain boundaries. Ergo, the scattering can be reduced if the initial particle size used in preparation of the material is being reduced to well below the visible light wavelengths (about 1/15 of the light wavelength or roughly 600/15 = 40 nm) [19].

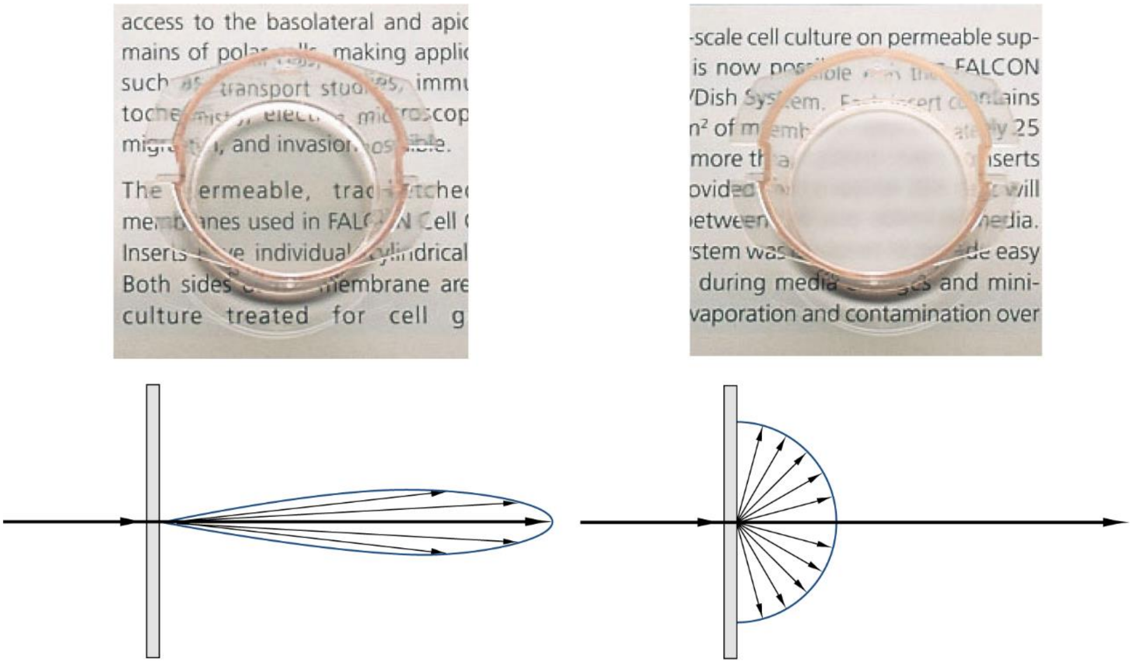

A) Narrow angle scattering **B) Wide angle scattering**

Figure 12: Light Transmission Mechanisms

2.5 Properties and applications of alumina nanofibers

Aluminum oxide or simply alumina with chemical formula Al_2O_3 is a well-known and intensively studied ceramic material that has a wide range of applications. High dielectric nature and being electrically insulator are its fundamental electrical properties, while high thermal stability, high hardness, and wear resistance make it one of the best candidates for catalyst support, filters, abrasive and thermal wear coatings, etc. Alumina exists in many metastable forms (transition alumina), such as γ-, δ-, η-, θ-, κ- phases and thermodynamically stable α- Al_2O_3 phase, which is the only stable form at any pressure and temperature [20][21].

One dimensional (1D) structures such as nanofibers and nanotubes exhibit unique properties that make them potential building blocks for the next generation nano-devices and emerging applications. Recent advances in research on 1D objects indicate that nanofibers with a range of predefined properties (such as size and shape, chemical composition and crystalline structure) can offer an excellent paradigm to develop novel functional device prototypes: catalyst support, chemical and bio-sensors, membranes, and nanofillers for advanced composites. The key step is a proper functionalization of the raw network of the fibers to meet requirements for their further application in novel nano-devices being beyond state-of-the-art. Among other ceramic nanostructures, fibers have unique geometrical parameters such as a high aspect ratio combined with a large surface area, which ensure wide usage of the fibers in different industrial applications. These nanostructures are the ideal candidates for filtration, catalysis and adsorption. Moreover, their large length to diameter and small mass to volume ratios make them promising candidates for reinforcing additives to form composite structures. Amongst the 1D nanomaterials, alumina nanofibers have drawn a noteworthy attention due to alumina specific properties such as high strength and stability at high temperatures (up to 1200 °C), low density and thermal conductivity, good corrosion resistance and electrical insulation. Studies utilizing γ-alumina nanofibers instead of traditional particulate γ-alumina are of tremendous interest for both fundamental research and technological application. However, to improve the targeted properties and/or to add new functionalities to alumina nanofibers (ANF) network, the well-developed process of functionalization is needed. Moreover, composite fibers may display a higher complexity and a wider range of properties as compared to non-functionalized materials. These characteristics are not only derived from the simple addition of properties of parent constituents but also result from their morphology and interfacial states. To further develop 1D functional nanofibers, the γ-alumina nanofibers network recently developed and produced in Estonia was functionalized by aluminum, zirconium, nickel, copper oxides. Metal oxides were homogeneously deposited onto high self-aligned network of alumina nanofibers in a single step by a novel strategy, where the network of nanofibers serve as a mesoporous reactive-template. This strategy involves combination of sol-gel, dip-coating and combustion synthesis methods. Urea and glycine as basic fuels and metal nitrate as precursor of metals and oxidant were used. [22]

Gamma alumina nanofibers used in this work were produced in Estonia with controlled liquid phase oxidation of aluminum for manufacturing of the alumina nanofibers (ANF) with extremely high aspect ratios of more than 107 and fiber diameter ranged from 5 to 50 nm. Fibers growth takes place at the interface of melt aluminum and ambient atmosphere. The method of crystal growth from a melt of metal is an excellent technique for preparing nanomaterials because of its low cost, high yield and the ability to achieve high purity of the oxide structures in the as-synthesized state. [23]

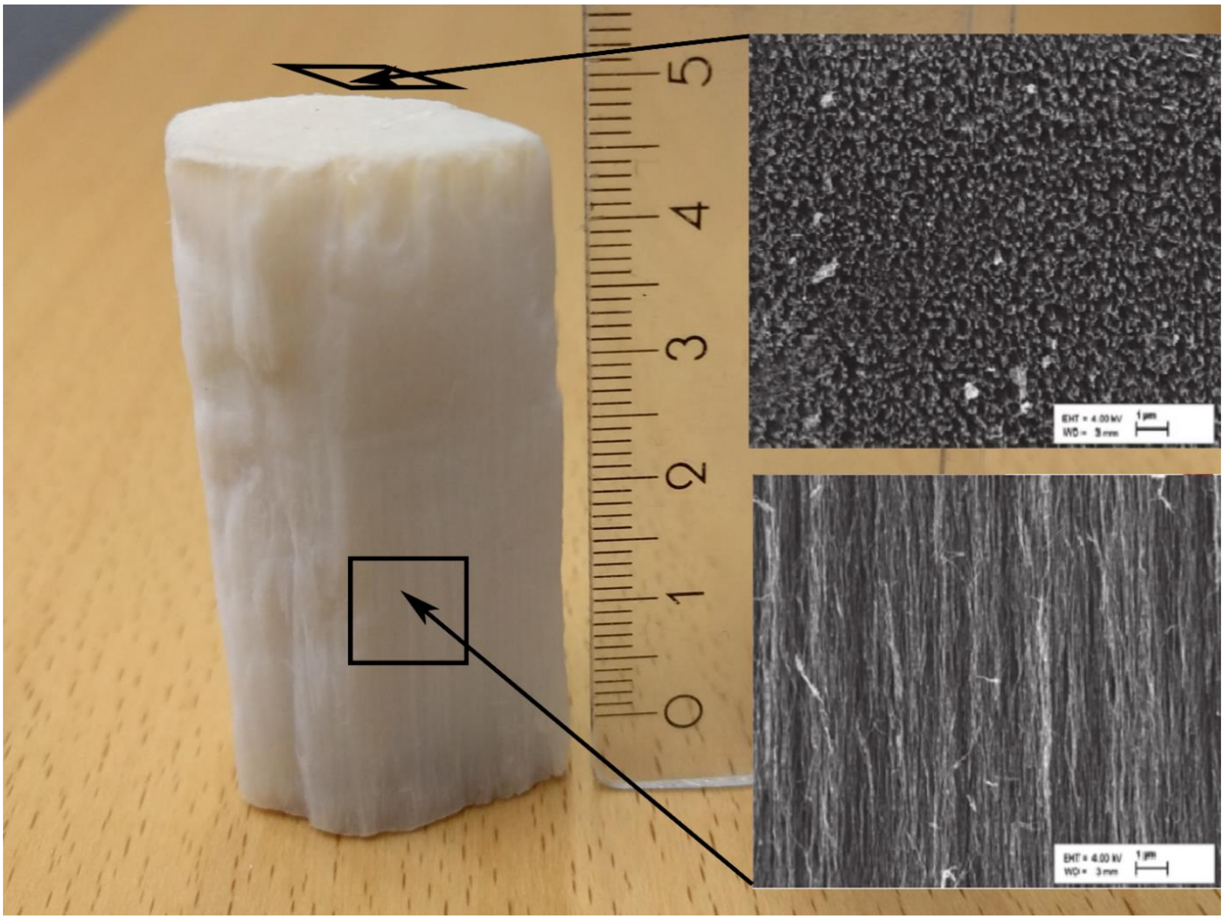

Figure 13: Alumina Nanofibers Produced in Estonia

2.6 Characteristics of the final product

2.6.1 Delafossite Copper Aluminate

Delafossite compounds belong to a family of ternary oxides with the general formula ABO_2. In this structure, the A cation is linearly coordinated to two oxygen ions and occupied by a noble metal cation which is nominally in the +1 oxidation state. Typical A cations include Pd, Pt, Cu, or Ag. The B cation is located in distorted edge-shared BO_6 octahedral with a central metal cation having a +3 charge. Cations fitting this requirement can be either p-block metal cations such as Ga, In, and Al; transition metal cations such as Fe, Co, and Y; and rare earth elements such as La, Nd, and Eu. The oxygen ion is in pseudo-tetrahedral coordination with one A and three B cations, as B_3AO. The delafossite structure can be visualized as consisting of two alternating layers: a planar layer of A cations in a triangular pattern and a layer of edge-sharing BO_6 octahedral flattened with respect to the c-axis. Depending on the orientation of each layer in stacking, the delafossite structure can form as one of two polytypes. By stacking the double layers with alternating A layers oriented 180° relative to each other, the hexagonal 2H type is formed. This structure has $P6_3/mmc$ space group symmetry. If the double layers are stacked with the A layers oriented the same direction relative to one another but offset from each other in a three-layer sequence, the rhombohedral 3R type is formed that has space group symmetry of $R\overline{3}m$ [24] [25]. Delafossite Copper Aluminum Oxide (CAO) along with other minerals of the ABO_2 group has been recognized for its electrical properties from insulation to metallic conduction. In this research work, delafossite $CuAlO_2$ with rhombohedral $R\overline{3}m$ crystal structure (Figure 14) is obtained.

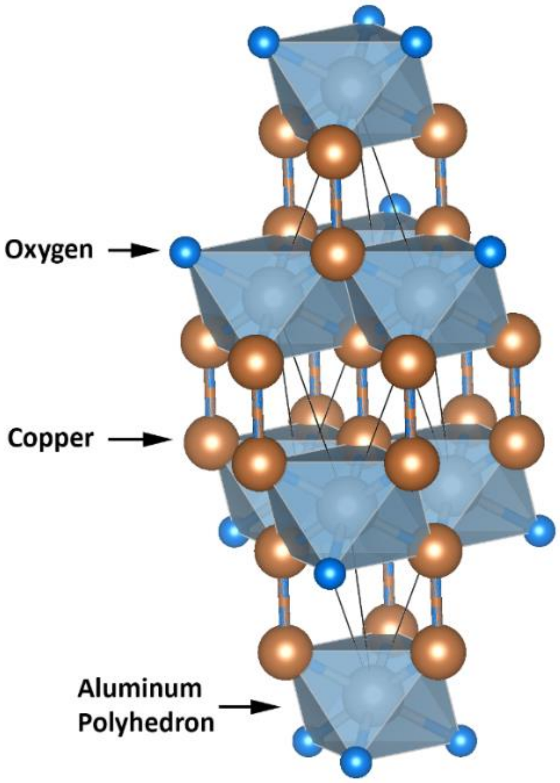

Figure 14: Rhombohedral $R\bar{3}m$ $CuAlO_2$ crystal structure

2.6.2 Spinel Copper Aluminate

Spinels are a class of minerals of general formulation AE_2O_4 which crystallize in the cubic (isometric) crystal system, with the oxide anions arranged in a cubic close-packed lattice and the cations A and B occupying some or all of the octahedral and tetrahedral sites in the lattice. Although the charges of A and B in the prototypical spinel structure are +2 and +3, respectively, other combinations incorporating divalent, trivalent, or tetravalent cations, including magnesium, zinc, iron, manganese, aluminum, chromium, titanium, and silicon, are also possible. The anion is normally oxygen; when other chalcogenides constitute the anion sublattice the structure is referred to as a thiospinel. Spinels are grouped in series by the B cation [26]. This is a very large family of compounds. They are not only widely-spread in nature occurring as pure (or mixed) minerals all over the globe; the spinels are also significant in many branches of technology and science. Many spinels are typical semiconductors with a rather narrow band gap (this is true especially for spinels containing the halogen atoms as anions), whereas the oxygen-based spinels have considerably wider band gaps and thus are typical dielectrics, which can be easily doped with rare earth and transition metal ions. For example, $MgAl_2O_4$ and $ZnGa_2O_4$ doped with Co^{2+}

ions were shown to be promising materials for solid state lasers; $MgAl_2O_4$ doped with Ni^{2+} ions was named as an active medium for the tunable infrared solid state laser. The spinel-based transparent ceramics for high-energy laser systems were designed recently [27]. Aluminum based spinels are a class of metal oxides with high thermal stability, high mechanical resistance, hydrophobicity and low surface acidity. Due to these properties, they have been used as catalysts in the decomposition of methane and the dehydration of saturated alcohols to olefins, as supports for the active metals, as pigments and as refractory or magnetic materials. Among the aluminate spinels, the copper aluminate ($CuAl_2O_4$) (Figure 15) is known to be active in the degradation of some organic compounds and in the reduction of NO with CO. The nanocrystalline copper aluminate has also been used as sensor material and as ceramic pigment for the production of ceramic coatings. Copper Aluminate spinels have high thermal stability, high mechanical resistance, hydrophobicity and low surface acidity. [28] [29]

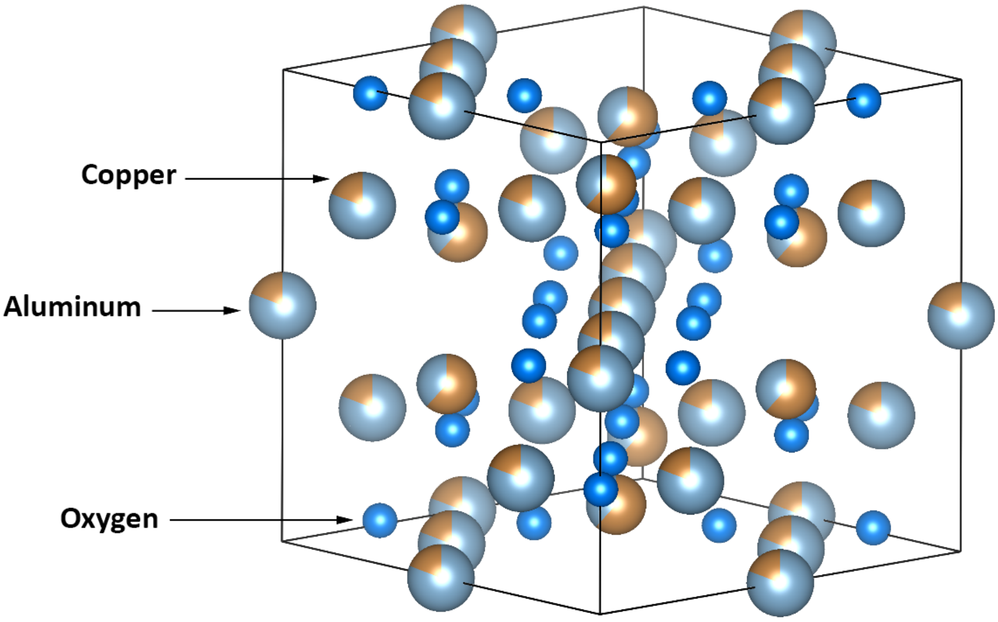

Figure 15: Cubic Fd $\overline{3}$m $CuAl_2O_4$ Crystal Structure

2.7 Pulsed Laser Deposition [PLD]

Pulsed Laser Deposition (PLD) system is a straightforward technique that makes the process of the film deposition very efficient and raises the ability of depositing a wide range of sublimable and non-sublimable materials (ceramics, etc.) materials in vacuum or under controlled gas flow. This technique uses a beam of laser with sufficient energy ranging from 150nm to 400nm. In order to achieve the necessary output power, the lasers are pulsed with rates up to 100Hz. Both excimer (e.g. KrF (At Warwick), ArF, XeCl) and solid state (e.g. Nd-YAG, Ruby) lasers are used in this technique. The beam of laser hits the solid target to ablates it and produce a plume of the material. The plume leaves the target perpendicular to its surface and being in plasma reaches the substrate which is positioned opposite to the target. A heated and rotating substrate option ensures uniform growth of the film. The ability of PLD to operate with high background pressure of reactive gasses (e.g. oxygen and nitrogen) is its most useful feature. This allows the stoichiometry of oxide targets to be maintained during grown of thin films. Moreover, in PLD the control of the stoichiometry of the film come from the ability to produce a target with the desired composition. [30] This triggered the PLD as the choice of deposition technique in this research.

In this work, a Neocera Pioneer 120PLD system with 248 nm UV excimer ArF laser, pulse energy up to 400 mJ, repetition rate of 20 Hz in average, and pulse duration of 20 ns was used. Maximum substrate temperature in this device can reach 900 °C and operating pressure range is 5×10^{-7} Torr to 500 mTorr.

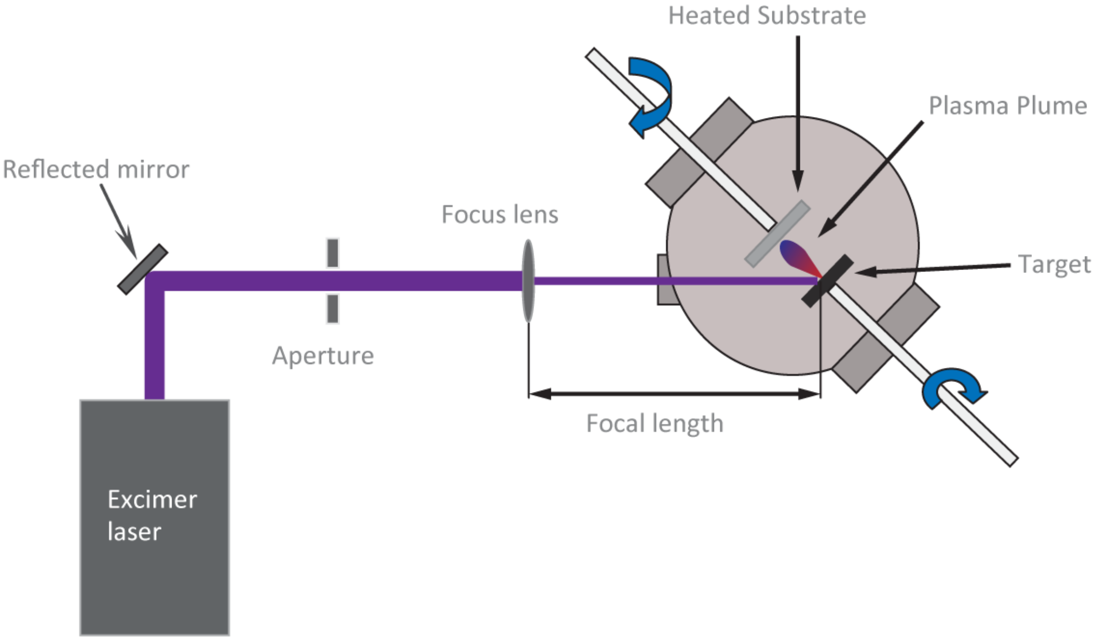

Figure 16: Schematic diagram of typical Pulsed Laser Deposition (PLD)

2.8 Objectives

The present research is motivated by the fact that production of delafossite copper aluminate is limited by the long-lasting, expensive, and sophisticated nature of the existing synthesis methods. Ultimately, broadening the application range of the material is directly connected with a combination of cost-effective, and scalable production route and exceptional functionality of the product.

The overall objective of the research work is to introduce a new resource friendly, and scalable method to produce delafossite copper aluminate being beyond reach with the conventional incremental material development. The introduced method includes reactive-dip coating approach using fibrous alumina network and copper nitrate as precursors. The work aims at optimization of the synthesis process of the $CuAlO_2$ for its further application as p-type transparent oxide semiconductor. Thus, the main activities of the work are as follow:

- Optimization of the synthesis parameters for controlling the composition and morphology of the designed product
    - Compositional and morphological characterization of the as-synthesized product
    - Investigate the reaction pathway
- Consolidate the obtained product by Spark Plasma Sintering (SPS) method
- Characterization of the bulk sample
    - Investigate the electrical resistivity, thermopower, and optical properties.
- Preparation of the target for Pulsed Laser Deposition (PLD)

Future Plans:

- Thin film deposition of the synthesized $CuAlO_2$ using PLD method
    - Characterization of the deposited films with XRD, SEM, Transmission Electron Microscopy (TEM), electrical resistivity measurement, and UV-Vis spectroscopy.
- Implementing photo-diode using ZnO as the n-type transparent semiconductor counterpart for the synthesized p-type $CuAlO_2$
    - Investigating the properties of the deposited heterostructure.

3. EXPERIMENTAL AND CHARACTRIZATION

3.1 Bulk Preparation

The approaches to synthesize copper alumina in this work are based on sol-gel process, dip coating and firing/wet combustion/heat treatment. The overall time of the bulk production process consists of 1 hour of aging and 1 hour of calcination. Schematic of the synthesis work flow is illustrated in Figure 17.

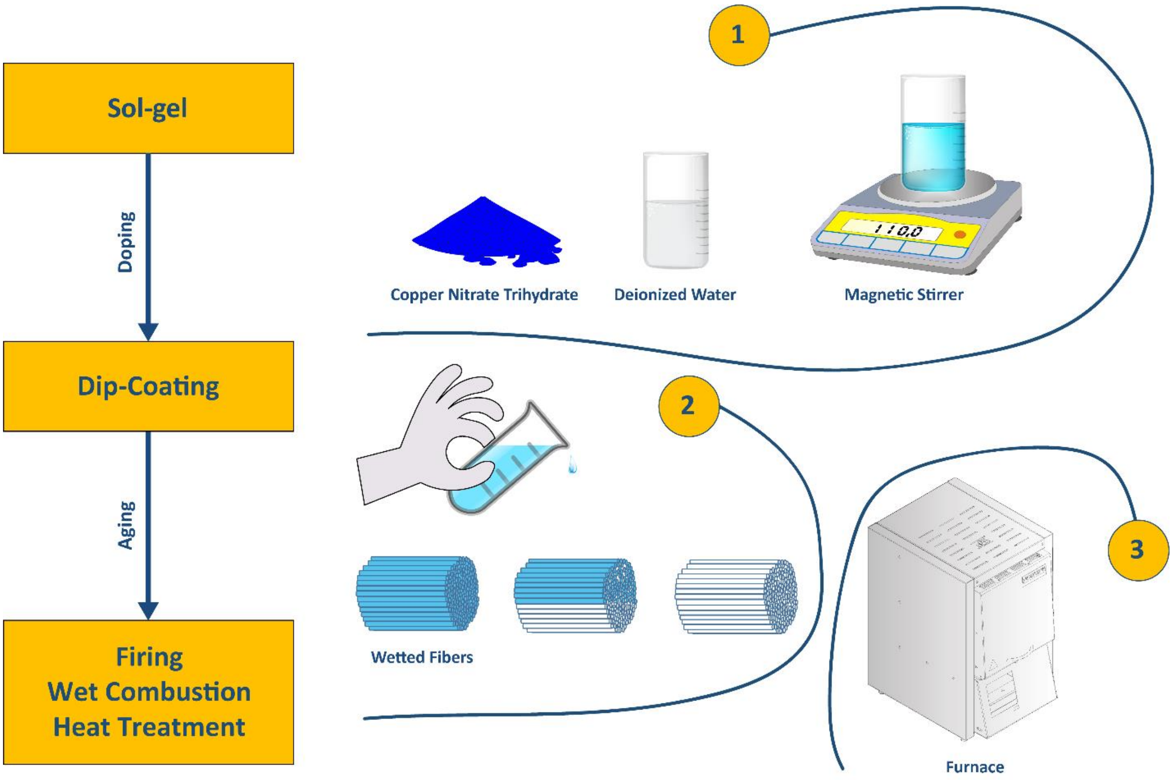

Figure 17: Schematic of the Synthesis Work Flow

3.1.1 Synthesis

The following reagents were used as the precursors: copper nitrate trihydrate [Cu $(NO_3)_2{\cdot}3H_2O$] (≥ 98%, Sigma-Aldrich) as the source of copper and oxidizer, glycine (≥99, Sigma) as organic fuels, and mesoporous network of self-aligned γ-alumina nanofibers (ANF) described in detail elsewhere [23] as source of aluminum. Two approaches have been applied to obtain copper aluminate: (i) dip coating and (ii) wet-combustion approaches.

(i) Reactive dip coating approach: A reactive solution was prepared dissolving 6 g of Cu (NO3)2·3H2O into 10 ml of distilled water. The obtained homogeneous reactive solution was dropped onto 1.5 g of bundled ANF and aged for 1 hour at room temperature for homogeneous

distribution of the solution all over the network of ANF due to capillary forces and epitaxial growth (Figure 18). The ratio of copper nitrate to ANF was 1.1/1 corresponding to stoichiometry amounts for production of $CuAlO_2$ (Equation 3). The reason for this additional copper nitrate was based on the proposal that surplus of CuO can act as flux agent in the reaction which improves and expedites the crystallization process. The surplus of CuO can be eliminated afterwards with rinsing the final product with nitric acid or hydrochloric acid based on the Equation 4 and Equation 5 reactions.

$$\mathbf{4\,Cu\,(NO_3)_2 + 2\,Al_2O_3 = 4\,CuAlO_2 + 8\,NO_2 + 3\,O_2}$$

Equation 3: Chemical Reaction for Synthesis of $CuAlO_2$

$$\mathbf{CuO + 2\,HNO_3 \rightarrow Cu(NO_3)_2 + H_2O}$$

Equation 4: Reaction with Nitric Acid

$$\mathbf{CuO + 2\,HCl \rightarrow CuCl_2 + H_2O}$$

Equation 5: Reaction with Hydrochloric Acid

The wetted network was heat-treated at 1150°C for 1 hour in a preheated furnace in air. Afterwards the baked sample was removed from the furnace (quenched in air) and characterized by different methods. Figure 18 (a).

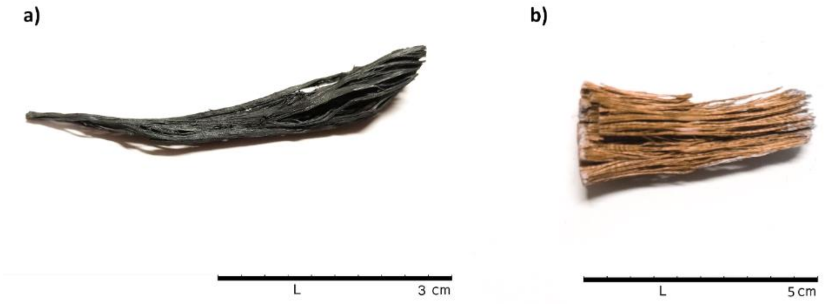

Figure 18: Photograph of a) final synthesis product of dip coating approach b) Final Product of Wet Combustion Synthesis Using Glycine as Fuel

<u>(ii) wet-combustion approach:</u> To prepare the reactive solution, 4.14 g of copper nitrate and 1 g of glycine (Equation 6) were dissolved in 14 ml of distilled water. The reactive solution was dropped onto the network of 2.5 g alumina nanofiber and left for homogenization for 1 hour. Later the sample was heat treated at 950 °C for 60 minutes in air. Product with a brown shade appeared at the end which is shown in Figure 18 (b).

$$\mathbf{13\,Cu\,(NO_3)_2 + 13\,Al_2O_3 + 2\,C_2H_5NO_2 = 13\,CuAl_2O_4 + 28\,NO_2 + 4\,CO_2 + 5\,H_2O}$$

Equation 6: Chemical Reaction for Synthesis of $CuAl_2O_4$

3.1.2 Consolidation and Sample Preparation

The synthesized copper aluminate in the section 3.1.1 (i) was grinded in a mortar, packed into 11 mm graphite die and sintered using a KCE®-FCT HP D 10-GB Spark Plasma Sintering [SPS] equipment by FCT Systeme GmbH (Rauenstein, Germany). A set of tests was performed to investigate the optimal sintering conditions taking into consideration the phase diagram of the compound to avoid liquid phase sintering and formation of metallic copper, or copper alumina phase change. The sintering conditions is summarized in Table 1. Conclusively, sintering condition was chosen as 950 °C with 50MPa force in vacuum. Subsequent to SPS, sample was cut into rectangular shape (8×4×3.5 mm) using a high-speed diamond saw. The rectangular samples later were annealed at 1100 °C for 24 hours to achieve grain growth and better interconnections at grain boundaries to support electrical conductivity, and thermopower measurements.

Code	Temperature (°C)	Force (MPa)	Atmosphere	Density (g/cm^3)	Composition
SPS-CA-1	850	40	Vacuum	3.11	No Change
SPS-CA-2	850	50	Vacuum	3.20	No Change
SPS-CA-3	900	50	Vacuum	3.69	No Change
SPS-CA-4	950	50	Vacuum	3.97	No Change
SPS-CA-5	1100	50	Vacuum	4.11	Metallic Copper

Table 1: Sintering Conditions

Separately for comparison, 3 samples were obtained using hydraulic press with following procedure: the as-synthesized dip-coated product was grinded in a mortar. The resulted fine powder was pressed under 5MPa hydraulic pressure and annealed at 500 °C and 800 °C. The 3rd sample remained unannealed to evaluate the effect of annealing on the phase composition, microstructure and electrical conductivity.

3.1.3 Ball Milling

After a preliminary grinding of the deep-coated copper aluminate in a mortar, the powder was packed in a polyethylene jar with zirconia balls of 0.8 and 0.3 mm in size. The ratio of the powder to grinding media was 1:5 and the dry milling was performed for 24 hours. After the ball milling the grinding media was removed using a 140 µm sieve and the size distribution of the powder particles was studied with SEM.

3.2 Thin Film Deposition

The delafossite copper aluminate synthesized with dip coating approach was considered as target material for thin film deposition using pulsed laser deposition (PLD) technique as a part of the future aims of this research project. Therefore, a target disk was prepared in a way to meet the requirements of the PLD device.

3.2.1 Target Preparation

The as-synthesized delafossite copper aluminate described in section 3.1.1 (i) was grinded in mortar and using SPS at 950 °C and 50 MPa was packed into a spherical sample (CA1) with 20 mm diameter and 3 mm thickness. The sample was later annealed and 1100 °C for 24 hours in order to eliminate impurities and achieve phase pure $CuAlO_2$.

3.2.2 Deposition Mechanism

To conduct the first set of experiments, glass substrate was cut into 1 cm^2 and cleaned in a sonication bath for 20 minutes using acetone and methanol each for 10 minutes. The cleaned substrates and CA1 target prepared in section 3.2.1 were used to grow thin films of $CuAlO_2$ at deposition temperature of 200 °C in high vacuum with 18000 pulses of 200 ms.

3.3 Characterization Techniques

Phase and microstructural analysis were carried out by using XRD, and SEM. The mechanism of the combustion process was investigated by using different in situ thermal techniques, including thermo-gravimetric analysis (TGA) and differential thermal analysis (DTA). Physical properties were investigated through electrical conductivity, Seebeck effect, UV-Visible, and Hall measurements.

3.3.1 X-ray Diffraction

XRD technique is a rapid analytical technique for studying chemical composition of materials, their crystal structure, crystallite size and atomic spacing. The x-ray diffraction pattern of a substance can be considered as a fingerprint of the substance which can be indexed and be used to match up with newly obtained patterns to identify them. X-ray emitted from a generator is directed at the target material. Scattering of this incoming incident occurs when x-ray photons collide with the electrons in the material. They interact in two different ways; coherent and incoherent. In the case of coherent scattering no energy of the incident photon is converted to kinetic energy in the medium and no change in wavelength happens (elastic scattering). The scattering is said to be incoherent if the wavelength of the incoming light incident is changed. These diffractions can be detected with photodiode to be used to generate a pattern as an identity footprint of the substance. The beams are diffracted at multiple angles due to the plane orientation of the crystals present in the material according to Bragg's law (Equation 7).

$$n\lambda = 2d\sin\theta$$

Equation 7: Bragg's Law

Where n is an integer, λ is the wavelength of incident wave, d is the distance between the planes in the atomic lattice, and θ is the angle between the scattering planes and incident ray. The data from the measured intensity and diffraction angles can be used to estimate the average crystallite size of the material using the Scherer equation (Equation 8).

$$\tau = \frac{k\lambda}{\beta cos\theta}$$

Equation 8: Scherrer Equation

In this equation τ is the mean size of the ordered (crystalline) domains, which may be smaller or equal to the grain size in nm, and k is a dimensionless shape factor with a value close to unity. The shape factor has a typical value of about 0.9, but varies with the actual shape of the crystallite. λ is the X-ray wavelength. β is the line broadening at half the maximum intensity (FWHM), after subtracting the instrumental line broadening, in radians. This quantity is denoted as 2θ, and θ is the Bragg's angle in degrees [31].

In this study, the product phase identification was performed by an X-ray diffraction using a PANanalytical model X'pert Pro diffractometer with CuKα radiation at 45 kV, 40 mA, and scan rate of 0.026 °/s within the angle range of 2θ = 5 - 90°.

3.3.2 Scanning Electron Microscopy

Scanning electron microscopy is a magnification technique that utilizes focused beams of electrons to obtain images from the substance structure and morphology. Since there is restricting limit for using photons with high energy or very small wavelengths, in SEM electrons are used in an accelerated magnitude with energies between 2-1000 keV which corresponds to wavelengths of 0.027 – 0.0009 nm. In principle, the elastic scattering event affects the trajectories of the beams of the electrons inside the specimen without altering the kinetic energy of the electron. This phenomenon is responsible for electron backscattering that forms the image signal in SEM. Inelastic scattering occurs due to the transfer of energy from beam of electrons to the atoms of the specimen leading to the generation of secondary electrons (Auger electrons) [32] [33]. In this study, scanning electron microscopy (SEM Zeiss EVO MA 15, Germany) equipped with EDS (energy dispersive X-ray spectrometer) with voltage of up to 20 kV and magnifications up to 50 kX was use.

3.3.3 Thermal Analysis

Thermal gravimetric analysis (TGA) is a method of thermal analysis in which physical changes in material are measured as a function of increasing temperature with isotropic, anisotropic or step function heating rate. In practice, weight of the sample is being recorded at each temperature/time steps. It is common to conduct this method together with differential thermal analysis (DTA) or differential scanning calorimetry (DSC) to compare both mass loss and temperature change in the sample material.

In this research the kinetics of the process were studied with simultaneous coupled thermal analysis (TG-DSC) with STA449C “Jupiter” (Netzsch Gerätebau GmbH. Experiments were performed in synthetic dry air (21% O_2, balance nitrogen; Linde AGA) flow of 20 ml/min with heating and cooling rates of 5°C/min.

3.3.4 Resistivity Measurement

The electrical conductivity was measured by a DC-four-probe (Figure 19) in air tight sample chamber method from 77 K to room temperature using liquid nitrogen and from room temperature to 400 K using a tube furnace in argon atmosphere. Samples prepared by different consolidation approaches were used in rectangular form (8.1×3.6×4.2) mm^3. The samples dimensions, measured with a Vernier caliper, weighed in an analytical balance, and values were used to estimate the bulk density. The measurement probes were connected to the samples using an Ag-conductive paste. DC current was generated using an Advantest R6144 programmable dc voltage/current generator and voltage was read using an Agilent 34420A Micro-Ohm meter. The voltage difference between the inner electrodes was read and the correspondent V/I value for resistance was recorded for every temperature point. Conductivity of the samples in Siemens per meter was calculated using (Equation 9) where σ is the conductivity L is the distance between inner electrodes, and A is the cross-section area of the sample.

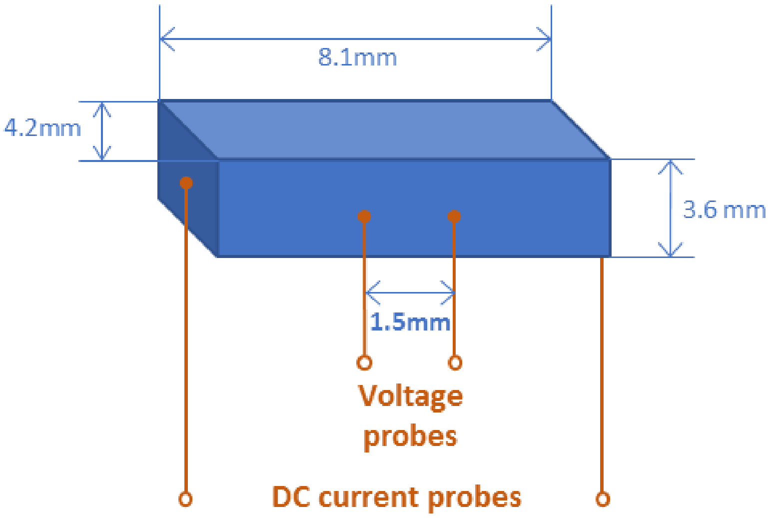

Figure 19: Schematic of the Electrical Conductivity Four-probe Setup

$$\sigma\ (Sm^{-1}) = \frac{\mathrm{L}(m)}{\mathrm{R}(\Omega).\,\mathrm{A}(m^2)}$$

Equation 9: Electrical Conductivity

3.3.5 UV-Visible Spectroscopy

Ultraviolet–visible spectroscopy is a technique to quantized absorption, transmission, and reflectance properties of materials in the portion of electromagnetic spectrum adjacent to the near-UV and near-infrared [NIR] wavelengths. In this region of the electromagnetic spectrum, atoms and molecules undergo electronic transitions, hence this phenomenon can affect the way the material deals with incoming wavelengths. Absorption spectroscopy is complementary to fluorescence spectroscopy which deals with transitions from the excited state to the ground state, while absorption measures transitions from the ground state to the excited state. Molecules/atoms containing π-electrons or non-bonding electrons (n-electrons) can absorb the energy in the form of ultraviolet or visible light to excite these electrons to higher anti-bonding molecular/atomic orbitals. The more easily electrons can be being excited (i.e. lower energy band gap between the HOMO/VBM and the LUMO/CBM), the longer the wavelength of light the material can absorb. To study optical properties of the bulk material in this research, diffuse reflectance spectrum was recorded with a LAMBDA 950 UV/Vis/NIR PerkinElmer Spectrophotometer UV–Vis spectrophotometer. The data was collected for the range 200-1000nm.

3.3.6 Thermoelectric Power Measurement

Thermoelectric properties of the material were studied by measuring the Seebeck coefficient S (=DV/DT) with respect to copper from 273 K to 400 K using a differential measurement method. In this method, which is described in detail elsewhere [34], at a stabilized temperature, a small temperature gradient is generated across the sample length, and the thermoelectric voltage is recorded using copper leads.

3.3.7 Hall Effect Measurement

If a thin flat conductor placed in a magnetic field while an electric current is passing through it, the magnetic field exerts a transverse force on the moving charge carriers pushing them to the sides of the conductor. This effect from the magnetic field becomes balanced with a buildup of charge at sides of the conductor which produces a measurable voltage between the two sides of the conductor. The voltage is called Hall voltage and can be used to determine the type of the charge carriers as well as their concentration and mobility. In this study, an electro magnet with maximum 1 Tesla of magnetic field which was equipped with a temperature control unit was used to conduct the Hall measurement from 273 K to 350 K. Hall coefficient, carriers' concentration, and carriers' mobility was determined using Equation 10, Equation 11, and Equation 12 respectively.

$$R_H = \frac{V_H \times t}{I \times B}$$

Equation 10: Hall coefficient R_H, Hall voltage V_H, thickness t, electric current I, and magnetic field B

$$n = \frac{1}{R_H \times e}$$

Equation 11: Carriers' concentration n, Hall coefficient R_H, and elemental charge e

$$\mu_n = \frac{\sigma}{n \times e}$$

Equation 12: Carriers' mobility μ_n, and electrical conductivity σ

4 RESULTS AND DISCUSSION

4.1 Microstructure and Crystal Structure

The X-ray diffraction pattern suggests formation of delafossite $CuAlO_2$ with rhombohedral R-3m crystal structure (Figure 14) at 1100 °C in our reactive dip coating approach as dominant phase accounting for more than 90% (Figure 20). Other phases present in the synthesized fibers are spinel $CuAl_2O_4$ and residue of CuO. A low degree of volume change is observable from the unit cell parameters as the cell volume after annealing at 1100 °C was decreased from 1.6% to 118.05 $Å^3$. This can be explained by the upper temperature stability limit of delafossite phase which is 1260 °C in air [35]. This phase is also thermodynamically unstable below 1000 °C in air, easily decomposing to the Cu^{2+} compounds; CuO, and $CuAl_2O_4$ [13]. Relative density of the spark plasma sintered sample measured with Archimedes method was 3.9 g/cm^3 which is 73% of the theoretical density calculated from the unit cell parameters. XRD patterns for as-prepared consolidated samples described in section 3.2 annealed at 500 °C, 800 °C, and 1100 °C is shown in Figure 21. It is observable that annealing at 500 °C does not affect phase purity and crystallinity of the materials whilst in the case of 1100 °C the phase purity slightly increased in favor of delafossite phase. The pattern for 800 °C annealed sample suggests phase change in a way that the dominant phases are the spinel $CuAl_2O_4$ and CuO. It is worth mentioning that calcination at 1100 °C in N_2 or vacuum resulted in formation of metallic copper (Figure 22).

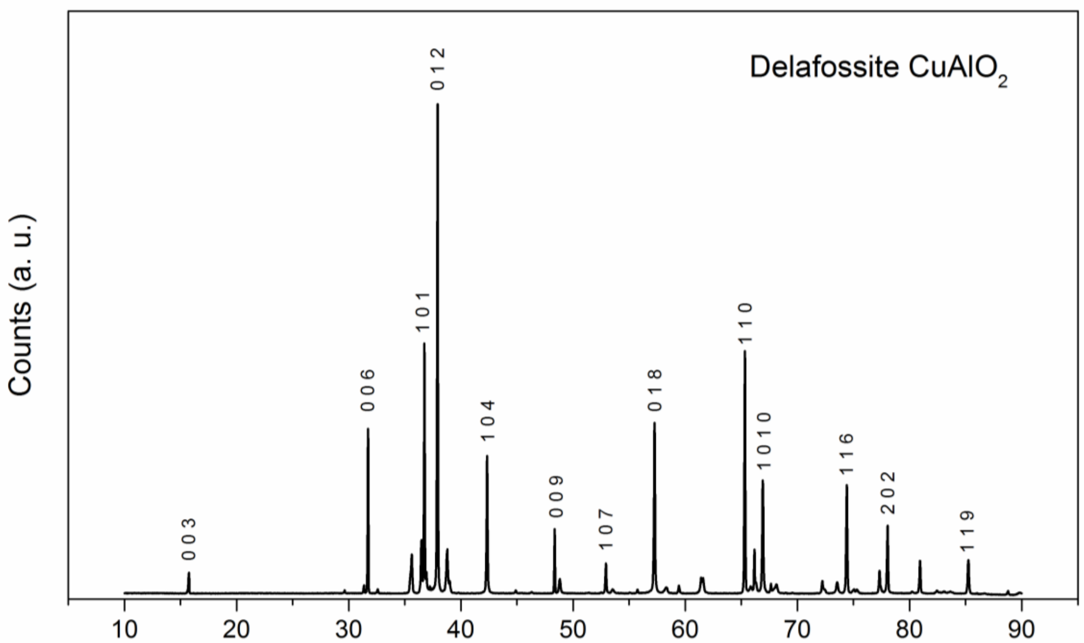

Figure 20: XRD pattern at 1100 °C indicating Delafossite copper alumina

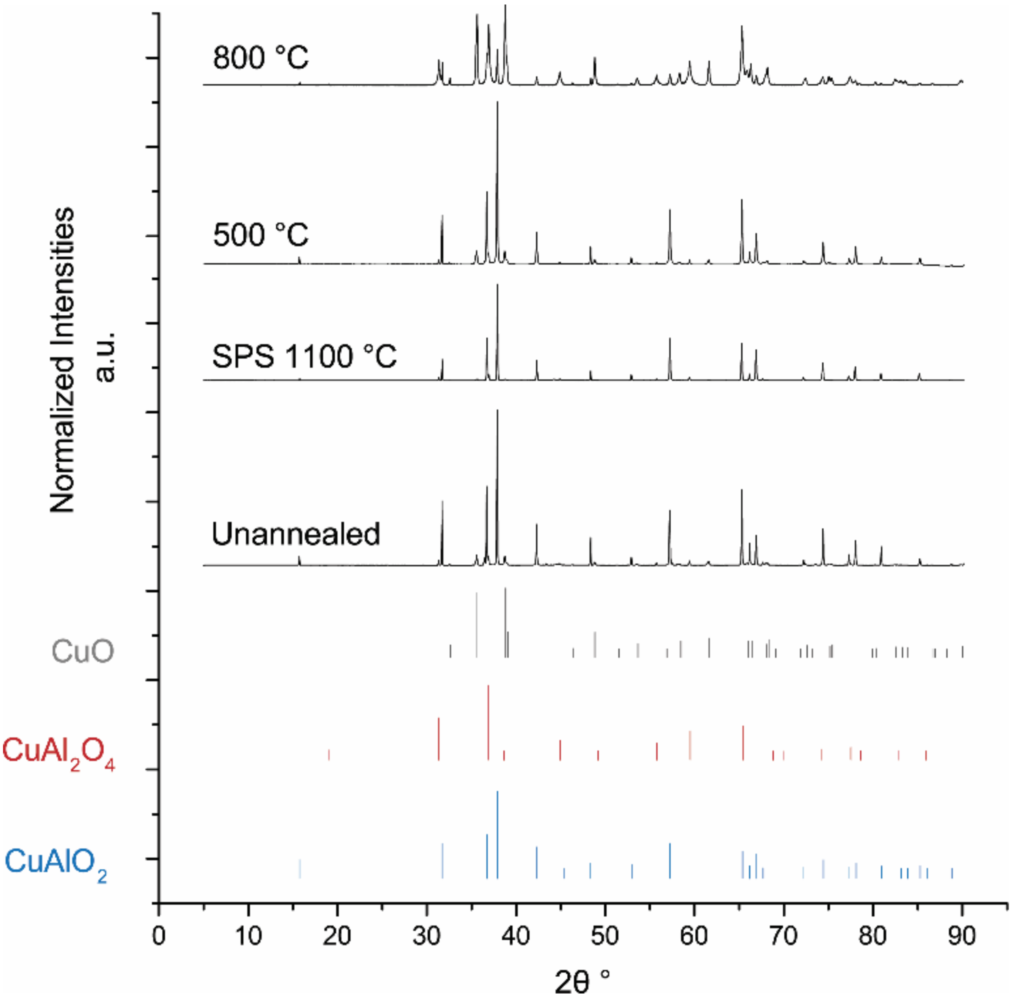

Figure 21: XRD pattern for different annealing approaches compared to reference peaks

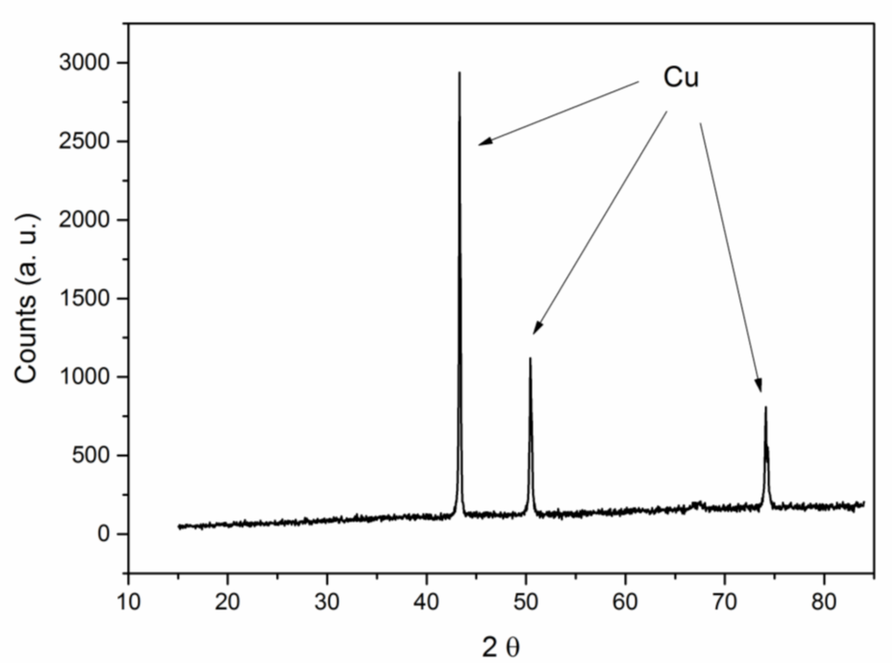

Figure 22: XRD pattern of the synthesis at 1100 °C in N_2

SEM microstructural analysis shows formation of polycrystalline grains in flaky boundaries for the bulk, with 50 µm average domain size (Figure 23). The preliminary grinding in a mortar resulted in powder with average particle size of 20 µm demonstrated in Figure 24. The crystallite size of 15 nm was estimated using XRD pattern of the powder and Scherrer's equation. Particle size distribution of the ball milled powder prepared in 3.1.3 was determined with SEM and is illustrated in Figure 25. The size distribution was ranging few hundreds of nanometers to few micrometers.

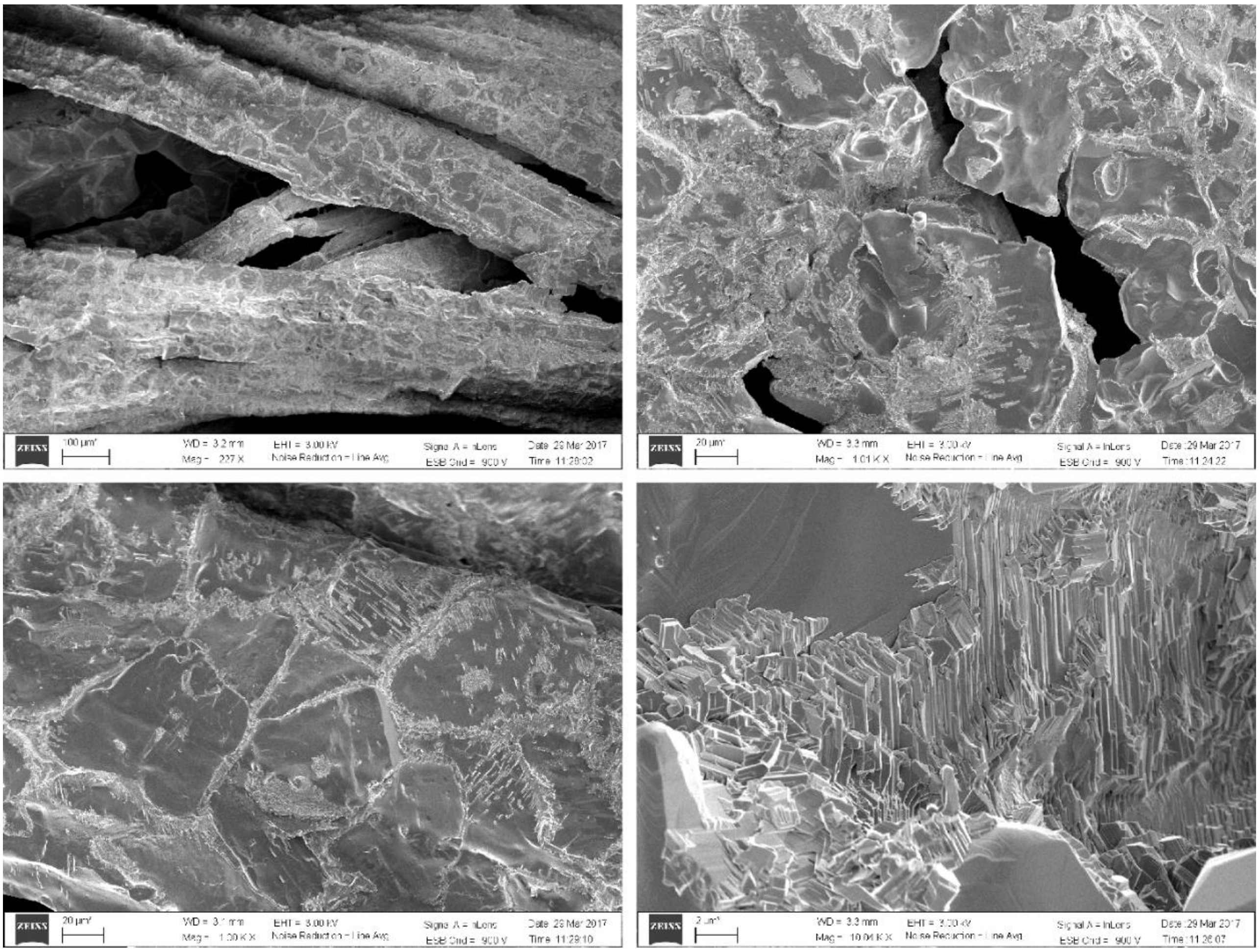

Figure 23: SEM micrograph of the Synthesized Bulk

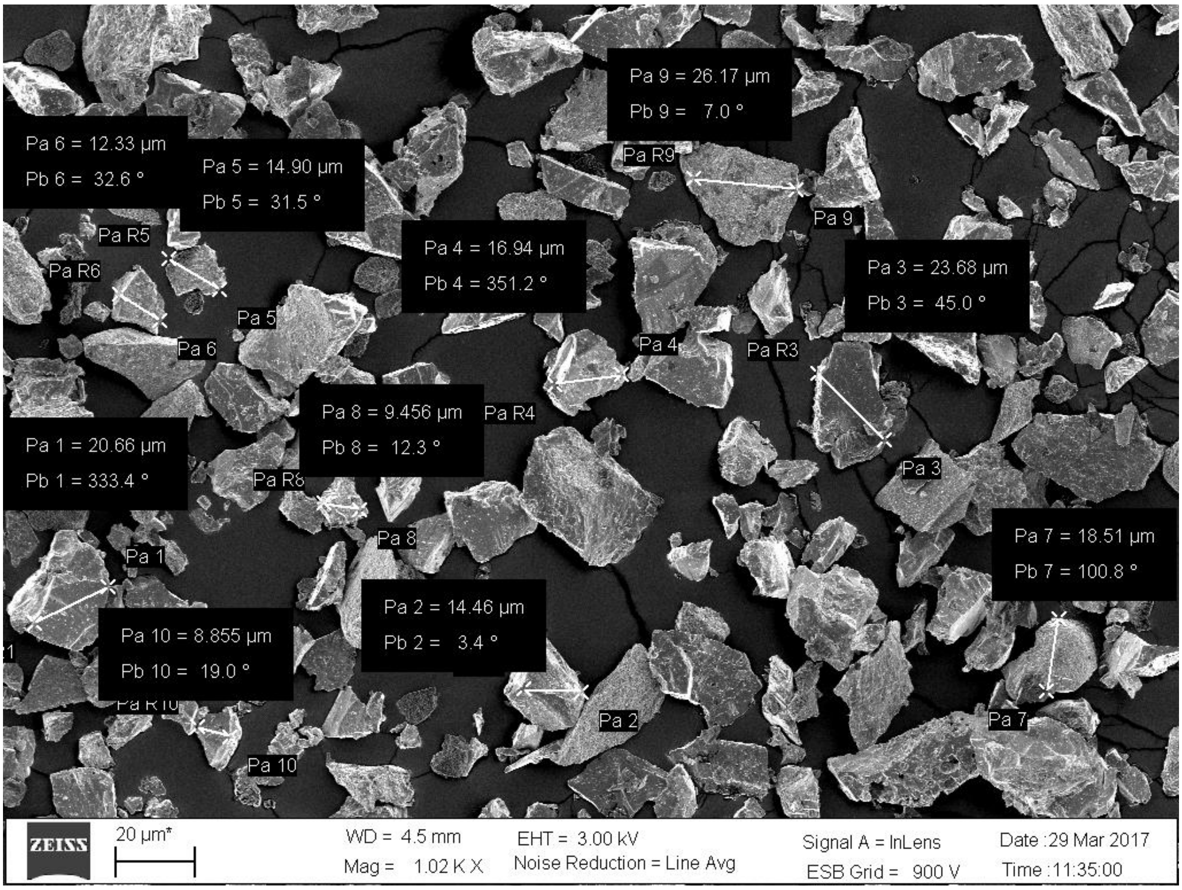

Figure 24: SEM Micrograph of the manually grinded powder

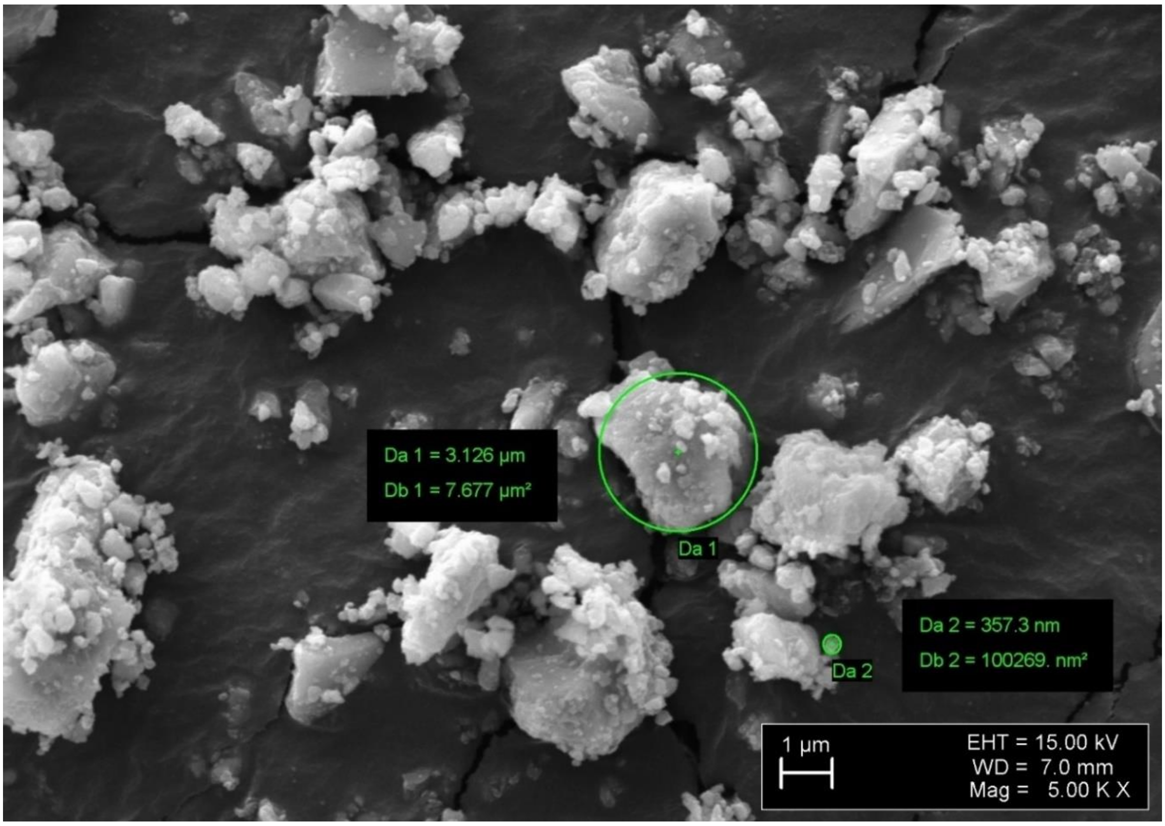

Figure 25: SEM Micrograph of the ball milled powder

X-ray diffraction pattern for the product of wet combustion approach at 950 °C using fuel, shows formation of spinel cubic $CuAl_2O_4$ as dominant phase. In contrast to the delafossite product, the spinel phase obtained from wet combustion method maintained its fibrous morphology as a result of lower calcination temperature. SEM micrograph of the spinel copper aluminate nanofibers is shown in Figure 26.

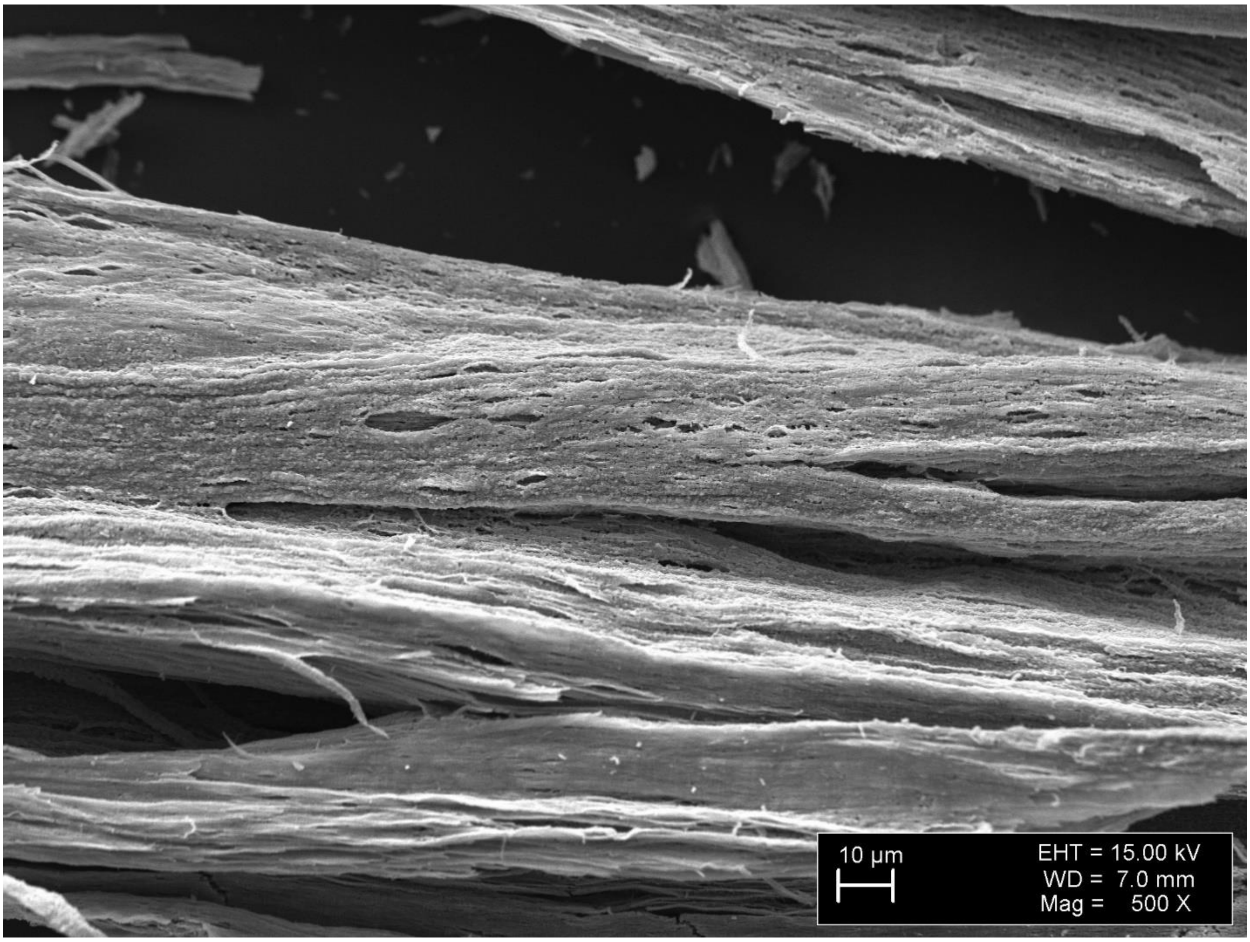

Figure 26: SME micrograph of spinel copper alumina nanofibers

XRD pattern of the thin film deposited at 200°C in vacuum Figure 27 shows single phase crystallized rhombohedral $CuAlO_2$. The (0 0 4) plane indicates c-axis orientation of the film which matches with the (0 0 8) plane of a peak observed at the same 2-theta in the target XRD pattern. The deposited film shows 85% transmission in the visible portion of the light spectrum.

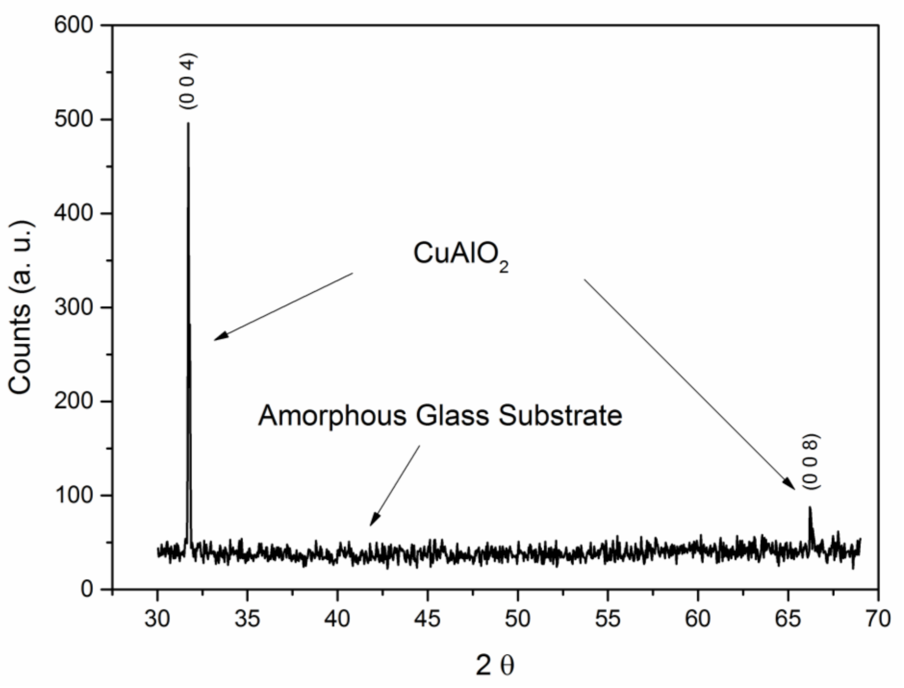

Figure 27: XRD pattern of the thin film grown at 200 °C in vacuum

4.2 Thermodynamics of the process

Temperature depended activation energy from 160 K to 400 K calculated from the electrical conductivity graph in Arrhenius Plot by multiplying the slope of the line to the Boltzmann constant estimated to be 0.26 eV (Figure 28).

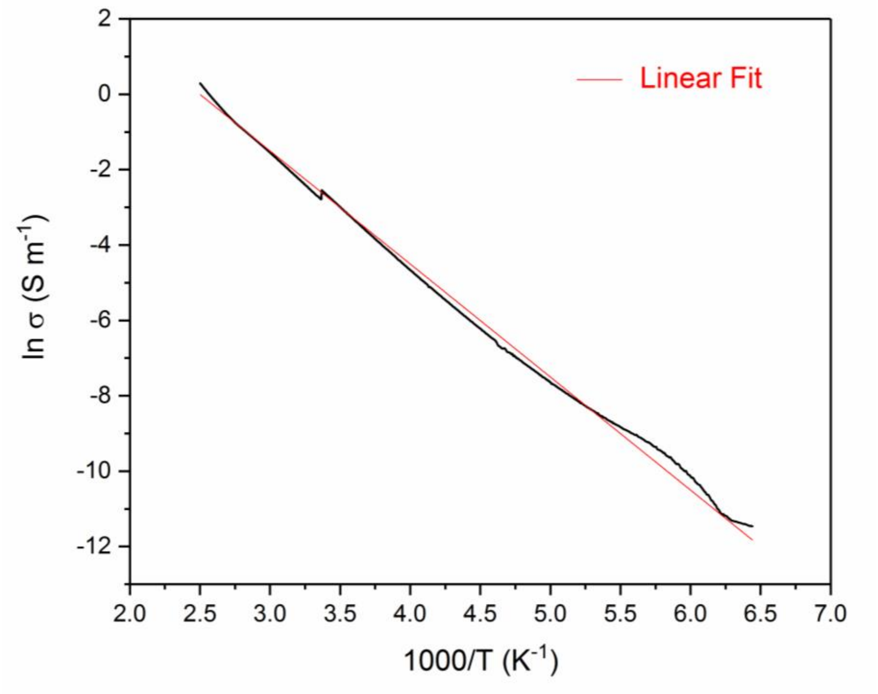

Figure 28: Activation Energy from Arrhenius Plot

The Figure 29 demonstrates thermal analysis of the sample consisting of Al_2O_3 nanofibers soaked by 1.1 stoichiometry amount of copper nitrate reactive solution. The DTA curve has three endothermic peaks at 115°C, 250°C and 1055°C. The DTG curve indicates that all of the endothermic peaks are accompanied by weight loss. The first endothermic peak at 115°C is two-fold and corresponds to the melting of copper nitrate trihydrate [36] followed by its decomposition and evaporation of chemically bonded water accompanied by a weight loss. The second endothermic peak at 250°C accompanied by weight loss corresponds to the thermal decomposition to CuO, which is in good agreement with Keely et al. [37] and releasing gases [38]. A moderate endothermic process is generated from 950 °C. According to Hu et al. [36] at this temperature formation of $CuAl_2O_4$ takes place, which turns to $CuAlO_2$ around 1000-1100 °C [39]. The abrupt endothermic peak at 1294 °C is the melting point of the compound [40].

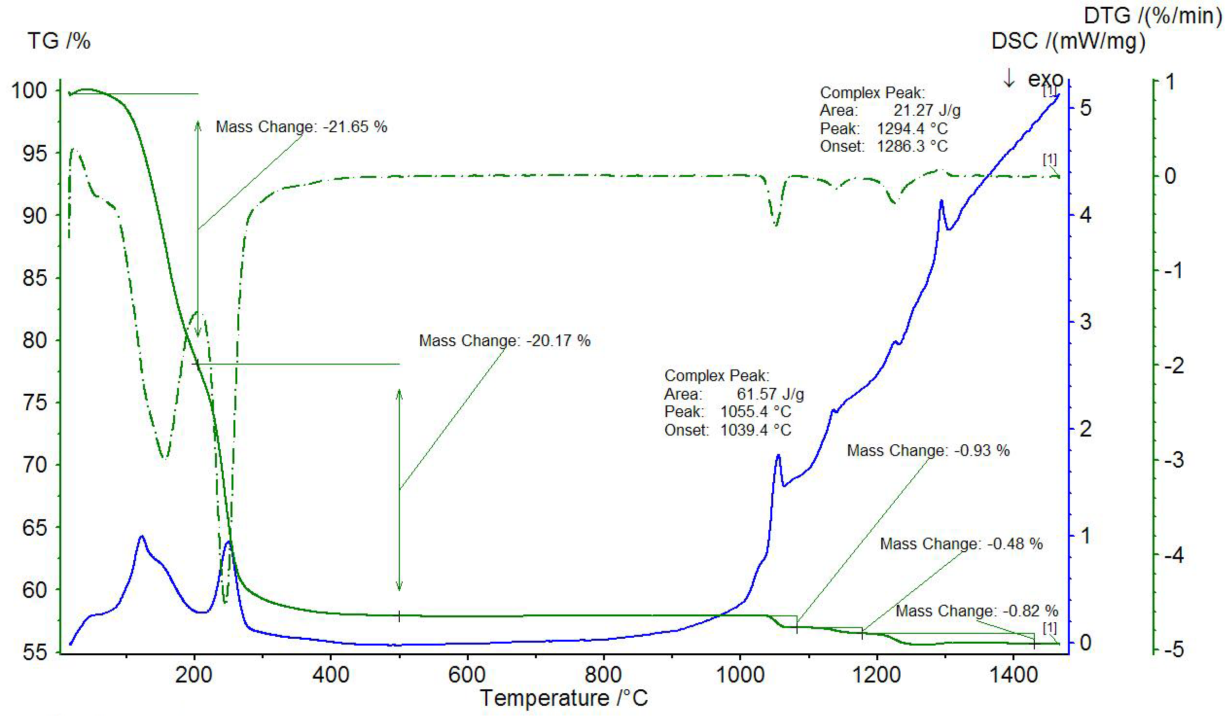

Figure 29: Thermal analysis curves of copper nitrate - alumina nanofibers

4.3 Electrical Conductivity

It is illustrated in Figure 30 that increase in annealing temperature has resulted in sharp increase in electrical conductivity. This can be a result of grain growth, reduction of contact pressure of metal oxide particles, and interfacial interdiffusion. Although according to XRD patterns, phase change to $CuAl_2O_4$ and CuO was occurred in the case of annealing at 800 °C, it showed second best conductivity in our measurements. The corresponding graphs indicate that the room temperature electrical conductivity is highest in the 1100 °C annealed sample. While the highest room temperature conductivity for bulk $CuAlO_2$ reported is 0.01 S cm^{-1} [40], this value was met at 380 K in our sintered-and-annealed-at-1100 °C sample with 72% of relative density.

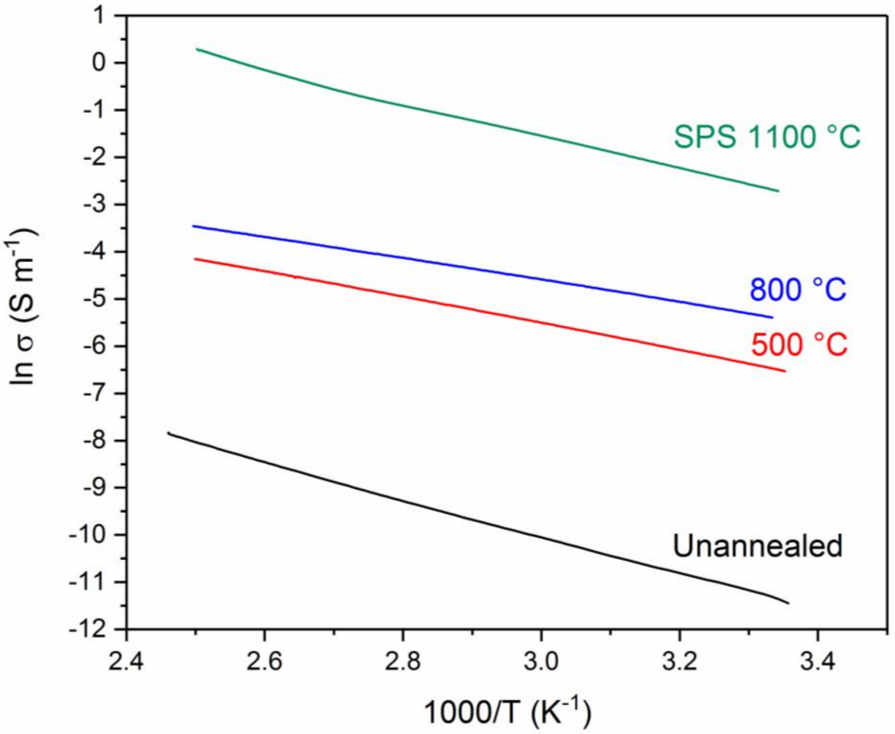

Figure 30: Conductivity of bulk $CuAlO_2$ samples with different compaction methods and annealing conditions.

4.4 Optical Properties

The diffuse reflectance spectroscopy has been used to determine the optical properties of sintered $CuAlO_2$. The direct optical band gap is determined by plotting Kubelka-Munk (k/s) versus energy (eV). Kubelka-Munk values are calculated with dividing molar absorption coefficient (k) (Equation 13) by scattering factor (s) (Equation 14). The linear portions of the graph are intercepted with trend lines which corresponds to the estimated energy band gap of 3.35 eV on the energy axis (Figure 31). This value meets the theoretical requirement for optical transparency.

$$k = (1 - R)^2$$

Equation 13: Molar Absorption Coefficient k, Reflectance (Absolute Values) R

$$s = R \times 2$$

Equation 14: Scattering Factor s, Reflectivity (Absolute Values) R

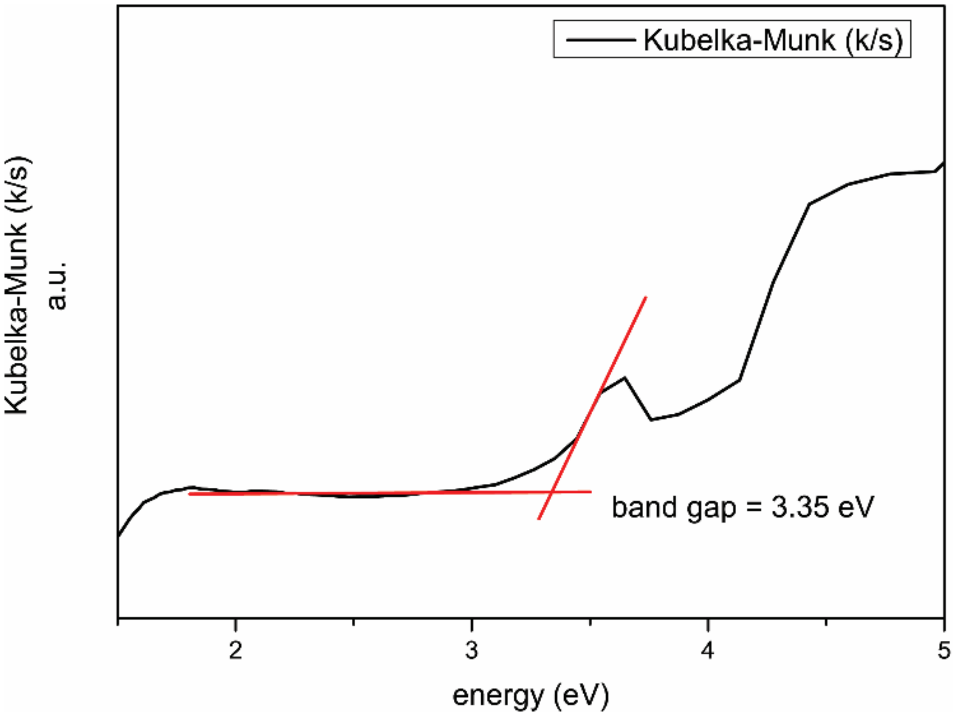

Figure 31: Diffuse reflectance data used in Kubelka-Munk method to estimate optical energy band gap of bulk CuAlO2.

Slight fluctuation in the result for the shorter wavelengths can be explained by existence of impurities and surface roughness of the bulk which impacts the scattering pattern.

4.5 Thermoelectric Power

Theoretical evidence suggests that a superlattice (2D and 1D) would enhance the thermoelectric figure-of-merit. Delafossite copper alumina possess natural superlattice (layered) structure which results in fairly high figure-of-merit. The reason for this finding is still unclear, but it should be associated with the correlation between the low dimensionality of a crystal structure and the behavior of electrons and phonons in an anisotropic structural environment [41]. Seebeck coefficient of the synthesized phase is demonstrated in Figure 32. The room temperature value was recorded as 360 μV K^{-1}. The temperature dependent thermopower has a minimum around 260 K for the consolidated $CuAlO_2$ sample. Below the mentioned temperature, significant fluctuations in the Seebeck coefficient is inevitable which is a result of increase in the sample's electrical resistivity as temperature decreases and from turbulent convection of air or from local variations in temperature (taking into account the 1mm thickness of the specimen). As a result, fluctuation in the voltage difference is also observed, which becomes a noise source [42]. The Seebeck coefficient decreases from 376 μV K^{-1} at 270 K to 347 μV K^{-1} at 345 K as a result of increase in charge carriers' concentration further proven in Hall measurement. The values rise again to reach 360 µV K^{-1} at 400 K. This behavior can be explained by dependency of the Seebeck coefficient in this temperature region on spin degeneracy and orbital degeneracy of the carriers whereas depending on their concentration [43]. Moreover, the impurities participation in electrical transport and mixed conduction can be an influencing factor.

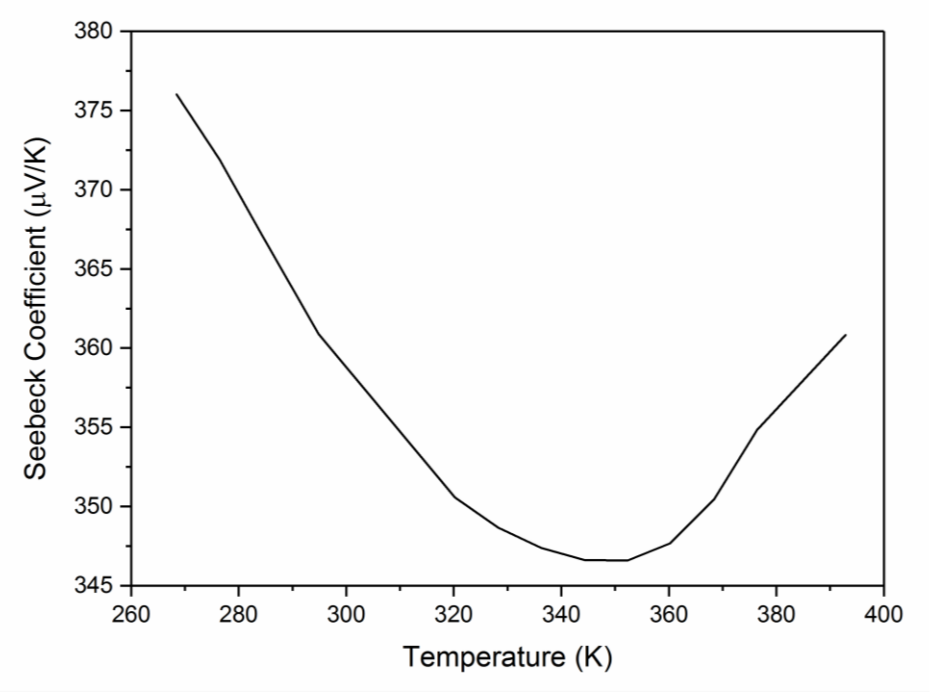

Figure 32: Seebeck Coefficient of synthesized $CuAlO_2$ (SPS sample annealed at 1100 °C)

Thermoelectric power of polycrystalline $CuAlO_2$ is reported with values ranging from 300 µV K^{-1} to 900 µV K^{-1} at different temperatures with relative densities ranging from 74% to 92% [40]. In our results, polycrystalline structure with 72% relative density generates 360 µV K^{-1} at 400 K with 1 Sm^{-1}. However, one must consider that Seebeck coefficient and electrical conductivity have a tradeoff; a higher Seebeck coefficient can be achieved by decreased carriers' concentration which results in reduced electrical conductivity [44]. The results show that the Seebeck coefficient is positive over the measured temperature range indicating p-type semiconducting behavior of the material. Power factor (P) was calculated using Equation 15 and is plotted versus temperature in Figure 33.

$$P = \frac{S^2}{\rho}$$

Equation 15: Power Factor P, Seebeck Coefficient S, Resistivity ρ

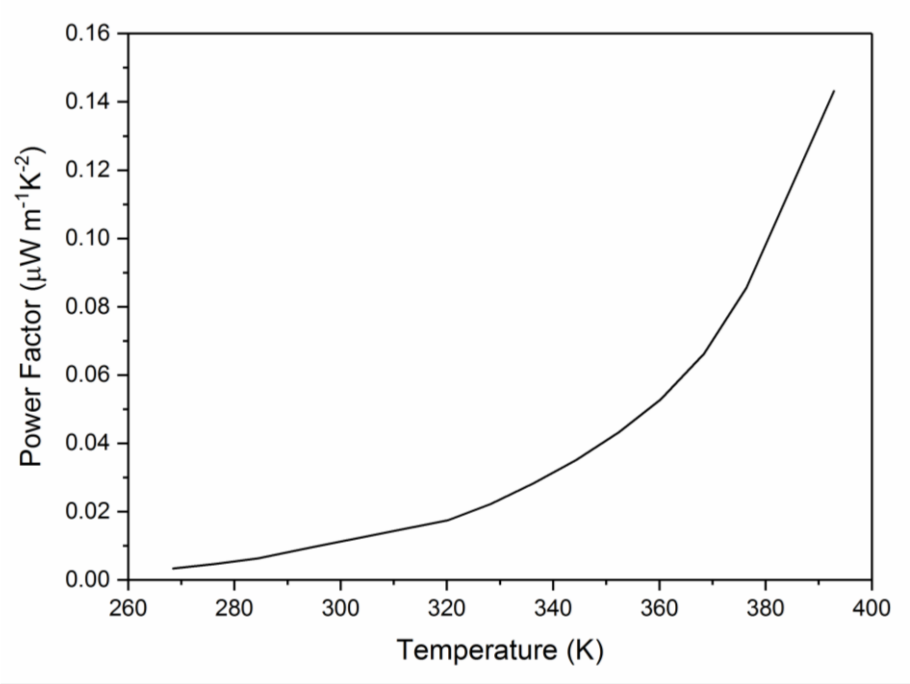

Figure 33: Power Factor of CuAlO$_2$ bulk sample

We demonstrated that in our measurement, Seebeck coefficient increased as the temperature increased over 340 K. This increase together with expected semiconducting nature of the material which reflects in decreased in resistivity as a result of higher carriers' concentration makes power factor rate of increase to be sharply positive after the same temperature check point. This can be explained by steady rates of change in carriers' concentration described before which eases the diffusion of high (excited by heat) and low energy carriers through the sample to reach equilibrium as the temperature gradient is applied.

4.6 Hall measurement

The Hall measurement revealed high hole mobility of 29.4 cm^2 V^{-1} s^{-1} in the bulk CuAlO$_2$ sample at room temperature while their concentration was 1.5×10^{18} per cm^3. The Figure 34 indicates drop in the carriers' concentration as the temperature reaches 273K which in fact is a result of crystal lattice contraction and correspondingly stronger interatomic bonds that reduces the number of the broken bonds (carriers) since there is less thermal energy available. On the other hand, a rise in the temperature to 320K results in Hall coefficient inversion. This phenomenon can be explained by the existence of two types of the charge carriers due to the presence of CuO impurities that become dominant at this temperature. Moreover, since the effective mass of the holes is much larger than that of electrons, the mobility of electrons becomes dominant at that temperature region due to the applied thermal excitation. Though, the number of the contributing carriers stays almost the same in the temperature region 320-360K which explains the steady region at the minima observed in Seebeck coefficient plot and does not show any conflict with the positive sign of the Seebeck coefficient in the same temperature region.

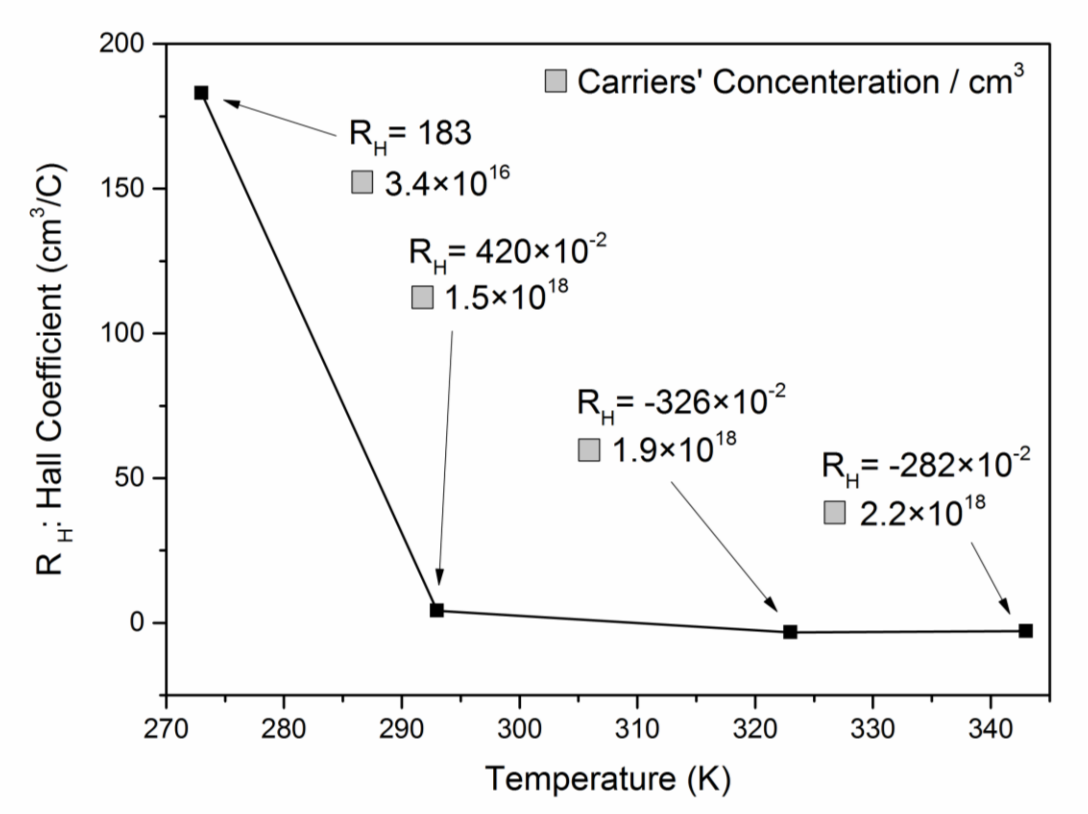

Figure 34: Hall coefficient vs. temperature for the bulk sheet of CuAlO$_2$

5. CONCLUSIONS

In this work, delafossite $CuAlO_2$ was successfully produced via a rapid reactive dip coating method base on alumina nano fibers for cumulative time of 2 hours of aging at room temperature and calcination at 1100 °C in air. X-ray diffraction spectra indicated rhombohedral delafossite $CuAlO_2$ as dominant phase. The synthesized bulk later was grinded and consolidated with spark plasma sintering and hydraulic press and annealed for 24 hours at different temperatures for comparison. The highest electrical conductivity was achieved in spark plasma sintered and annealed at 1100 °C sample. Room temperature resistivity of 0.07 S m^{-1} with direct optical band gap of 3.35 eV were determined with four probe measurement and UV-Vis spectroscopy respectively, while the activation energy was 0.26 eV over the temperature region of 77 K to 400 K. Thermoelectric power measurement confirmed the p-type semiconducting nature of the material and Seebeck coefficient at room temperature was 364 μV K^{-1} for a sample with 72% relative density. Temperature dependency of power factor was investigated from 270 K to 400 K and showed values from 0.0033 to 0.14 μW m^{-1} K^{-1} respectively. Determined by Hall measurement, the majority of the charge carriers were holes which shown mobility of 29.4 cm^2 V^{-1} s^{-1} while their concentration was 1.5×10^{18} per cm^3 at room temperature. Synthesized polycrystalline material is a proper candidate for p-type transparent film which can be used in different heterojunction implementations. Moreover, relatively high thermopower at different temperatures makes them good candidates for thermopower application such as residual heat to electricity. A spherical consolidated bulk was prepared from the synthesized $CuAlO_2$ and was used as target in pulsed laser deposition. Thin film of the material was grown on glass at 200 °C in high vacuum. X-ray diffraction spectrum indicated the c-axis oriented crystalline structure of the $CuAlO_2$ film.

6. Résumé

Since the discovery of delafossite $CuAlO_2$ as the first p-type Transparent Oxide Semiconductor (TOS) by Kawazoe et al. in 1997, several methods were introduced to synthesize them. A combination of p-type and previously discovered n-type transparent semiconductors revolutionized the opto-electronic device technology and lead to implementation of functional windows, transparent solar cells, light-emitting diodes, field electron emitters, etc. The delafossite-structured $CuAlO_2$ has attracted an immense research interest because of its interesting properties. To date, the $CuAlO_2$ films are found to have the visible-light transmittance as high as 80%, and can be considered as an ideal candidate for transparent p-type semiconducting applications without intentional doping. The $CuAlO_2$ can be used as photo catalyst for water splitting in visible light region in solar energy systems. Moreover, its natural super lattice structure makes it a suitable candidate for thermopower applications.

In this work, fabrication of $CuAlO_2$ by reactive dip-coating is proposed. The synthesis parameters that affect the crystal formation processes and the product morphology and composition, including the selection of starting materials and their molar ratios, temperature, pressure, and reaction time were studied. Delafossite $CuAlO_2$ was successfully synthesized from mesoporous network of γ-Alumina Nanofibers soaked by copper nitrate solution and calcined at 1100°C.

The chemical composition, morphology, thermal, electrical, optical properties, and synthesis mechanisms of $CuAlO_2$ also were studied. SEM microstructural analysis shows formation of polycrystalline $CuAlO_2$ with 20 µm average grain size which after ball milling reduced to few hundreds of nanometres. Crystallite size was estimated using XRD pattern of the powder and Scherrer'r equation to be 15 nm. Spark Plasma Sintering (SPS) was used to consolidate the powder under 50 MPa force at 950 °C in vacuum. Electrical conductivity measurement indicates room temperature conductivity of 0.07 Sm^{-1} which expands to 1 Sm^{-1} at 400 K. Activation energy from 77 K to 400 K shows a value of 0.26 eV. Optical band gap of the material was estimated from diffuse reflection data as 3.35 eV. Seebeck coefficient at room temperature was 360 $\mu V\ K^{-1}$ with power factor value of 0.01 $\mu W\ m^{-1}\ K^{-1}$ which rapidly expanded to 0.14 $\mu W\ m^{-1}\ K^{-1}$ as temperature reaches 400 K. A thin film of the as-synthesized copper aluminate was grown on glass using Pulsed Laser Deposition (PLD) technique at deposition temperature of 200 °C in high vacuum. The XRD pattern suggests formation of c-axis oriented rhombohedral $CuAlO_2$.

7. Resümee

Pärast seda, kui Kawazoe et al. avastasid 1997. aastal delafosiit $CuAlO_2$ kui esimese p-tüüpi läbipaistva oksiidpooljuhi (TOS), töötati nende sünteesimiseks välja mitmed meetodid. P-tüüpi ja varem avastatud n-tüüpi läbipaistvate pooljuhtide kombinatsioon muutis täielikult optoelektrooniliste seadmete tehnoloogiat ja viis funktsionaalsete akende, läbipaistvate päikeseelementide, valgusdioodide, välja elektronemitterite jms. rakendamiseni. Oma atraktiivsete omaduste tõttu on delafosiidi struktuuriga $CuAlO_2$ sattunud suure teadushuvi keskmesse. Tänaseks on leitud, et $CuAlO_2$ kilede nähtava valguse läbivustegur on lausa 80% ning need sobivad ideaalselt kasutamiseks lisanditeta läbipaistvates p-tüüpi pooljuhtrakendustes. $CuAlO_2$ saab kasutada fotokatalüsaatorina päikeseenergiasüsteemide nähtava valguse osas vee lõhustamiseks. Lisaks sobib see oma loomuliku supervõrestruktuuri tõttu ka termoelektrilise võimsuse rakendustesse.

Käesolevas töös pakutakse $CuAlO_2$ tootmiseks välja reaktiivse sukelduspindamise meetod. Töö käigus uuriti kristallisatsiooni protsesse ja toote morfoloogiat mõjutavaid sünteesi parameetreid, sealhulgas lähtematerjalide ja nende molaarsuhte, temperatuuri, rõhu ja reaktsiooniaja valik. Delafosiit $CuAlO_2$ sünteesiti edukalt mesopoorsest γ-alumiiniumoksiidist nanokiudvõrgust, mida leotati vasknitraadi lahuses ja kaltsineeriti temperatuuril 1100°C.

Samuti uuriti $CuAlO_2$ keemilist koostist, morfoloogiat, soojuslikke, elektrilisi, optilisi omadusi ja sünteesimehhanisme. XRD ja SEM analüüsiga moodustus 20 µm tera keskmise suurusega polükristalliline $CuAlO_2$, mis redutseeriti pärast kuulfreesimist mõnesaja nanomeetrini. Pulbri XRD mustrit ja Scherreri võrrandit kasutades saadi domeeni suuruseks 15 nm.

Pulbri konsolideerimiseks kasutati vaakumis 50 MPa sädepaagutust temperatuuril 950°C. Elektrijuhtivuse mõõtmine näitab toatemperatuuril juhtivust 0.07 Sm^{-1}, mis 400 K juures suureneb 1 Sm^{-1}. Aktiveerimisenergia 77 K kuni 400 K puhul on väärtuseks 0.26 eV. Materjali optiline keelutsoon hajupeegelduse andmete põhjal oli 3.35 eV. Seebecki koefitsient toatemperatuuril oli 360 $\mu V\ K^{-1}$ võimsusteguri väärtusega 0.01 $\mu W\ m^{-1}\ K^{-1}$, mis suurenes kiiresti 0.14 $\mu W\ m^{-1}\ K^{-1}$, kui temperatuur jõuab 400 K. Klaasil kasvatati impulsslasersadestust (PLD) kasutades kõrgvaakumis sadestustemperatuuril 200°C õhuke sünteesitud vask-aluminaadi kile. XRD muster lubab eeldada c-telje suunalise romboeedrilise $CuAlO_2$ moodustumist.

8. REFERENCES.

[1] Hiroshi Kawazoe, Masahiro Yasukawa, Hiroyuki Hyodo, Masaaki Kurita, Hiroshi Yanagi, and Hideo Hosono, “P-type electrical conduction in transparent thin films of CuAlO2,” *Lett. to Nat.*, vol. 389, no. 6654, pp. 939–942, Oct. 1997.

[2] H. Hosono, “Recent progress in transparent oxide semiconductors: Materials and device application,” *Thin Solid Films*, vol. 515, no. 15 SPEC. ISS., pp. 6000–6014, 2007.

[3] G. Rupprecht, “Untersuchungen der elektrischen und lichtelektrischen Leitf�higkeit d�nner Indiumoxydschichten,” *Zeitschrift f�r Phys.*, vol. 139, no. 5, pp. 504–517, Oct. 1954.

[4] T. Ishiguro, N. Ishizawa, N. Mizutani, and M. Kato, “High temperature structural investigation of the delafossite type compound CuAlO2,” *J. Solid State Chem.*, vol. 41, no. 2, pp. 132–137, 1982.

[5] M. Yu, G. Natu, Z. Ji, and Y. Wu, “p-Type Dye-Sensitized Solar Cells Based on Delafossite CuGaO 2 Nanoplates with Saturation Photovoltages Exceeding 460 mV,” *J. Phys. Chem. Lett.*, vol. 3, no. 9, pp. 1074–1078, May 2012.

[6] H. Gong, Y. Wang, and Y. Luo, “Nanocrystalline p -type transparent Cu–Al–O semiconductor prepared by chemical-vapor deposition with Cu(acac)2 and Al(acac)3 precursors,” *Appl. Phys. Lett.*, vol. 76, no. 26, pp. 3959–3961, Jun. 2000.

[7] K. Tonooka, K. Shimokawa, and O. Nishimura, “Properties of copper–aluminum oxide films prepared by solution methods,” *Thin Solid Films*, vol. 411, no. 1, pp. 129–133, May 2002.

[8] G. Li *et al.*, “Preparation and characterization of CuAlO2 transparent thin films prepared by chemical solution deposition method,” *J. Sol-Gel Sci. Technol.*, vol. 53, no. 3, pp. 641–646, 2010.

[9] S. Zhao, M. Li, X. Liu, and G. Han, “Synthesis of CuAlO2 nanofibrous mats by electrospinning,” *Mater. Chem. Phys.*, vol. 116, no. 2–3, pp. 615–618, 2009.

[10] T. V. Thu *et al.*, “Synthesis of delafossite CuAlO2 p-type semiconductor with a nanoparticle-based Cu(I) acetate-loaded boehmite precursor,” *Mater. Res. Bull.*, vol. 46, no. 11, pp. 1819–1827, 2011.

[11] J. Ahmed *et al.*, “Scalable synthesis of delafossite CuAlO2 nanoparticles for p-type dye-sensitized solar cells applications,” *J. Alloys Compd.*, vol. 591, pp. 275–279, Apr. 2014.

[12] M. D. Earle, “Electrons and holes in semiconductors,” *J. Franklin Inst.*, vol. 252, no. 1, p. 95, Jul. 1951.

[13] J. J. SPARKES, “Conduction in Semiconductors,” in *Junction Transistors*, Elsevier, 1966, pp. 1–34.

[14] B. L. Mitlyng and R. a Ganz, “Understanding the GERD.,” *Minn. Med.*, vol. 95, no. 4, pp. 42–5, Apr. 2012.

[15] M. A., O. Gonzlez, and J. R., “Optical Fiber Sensors for Chemical and Biological Measurements,” in *Current Developments in Optical Fiber Technology*, InTech, 2013.

[16] F. Albregtsen, “Reflection, refraction, diffraction, and scattering,” pp. 1–82, 2008.

[17] E. Goals, “Reflection and Refraction.”

[18] F. Jentoft, “Diffuse Reflectance IR and UV-vis Spectroscopy Modern Methods in Heterogeneous Catalysis,” *Mod. Methods Heterog. Catal.*, pp. 1–56, 2004.

[19] K. Tsukuma, I. Yamashita, and T. Kusunose, “Transparent 8 mol% Y2O3-ZrO2 (8Y) ceramics,” *J. Am. Ceram. Soc.*, vol. 91, no. 3, pp. 813–818, 2008.

[20] W. Ahmed, M. R. Noor El-Din, A. A. Aboul-Enein, and A. E. Awadallah, “Effect of textural properties of alumina support on the catalytic performance of Ni/Al2O3 catalysts for hydrogen production via methane decomposition,” *J. Nat. Gas Sci. Eng.*, vol. 25, no. February, pp. 359–366, Jul. 2015.

[21] M. Ridzuan and K. Yong, “Synthesis of Alumina Nanofibers and Composites,” in *Nanofibers*, no. February, InTech, 2010, pp. 405–418.

[22] M. Aghayan, *Functionalization of Alumina Nanofibers with Metal Oxides*. .

[23] M. Aghayan, I. Hussainova, M. Gasik, M. Kutuzov, and M. Friman, “Coupled thermal analysis of novel alumina nanofibers with ultrahigh aspect ratio,” *Thermochim. Acta*, vol. 574, no. October, pp. 140–144, Dec. 2013.

[24] M. Miclau, D. H. Ursu, S. Kumar, and I. Grozescu, “Hexagonal polytype of CuCrO2 nanocrystals obtained by hydrothermal method,” *J. Nanoparticle Res.*, vol. 14, no. 9, pp. 2–9, 2012.

[25] M. A. Marquardt, N. A. Ashmore, and D. P. Cann, “Crystal chemistry and electrical properties of the delafossite structure,” *Thin Solid Films*, vol. 496, no. 1, pp. 146–156, 2006.

[26] R. J. Hill, J. R. Craig, and G. V. Gibbs, “Systematics of the spinel structure type,” *Phys. Chem. Miner.*, vol. 4, no. 4, pp. 317–339, 1979.

[27] M. W. Tingley, R. L. Wilkerson, C. A. Howell, and R. B. Siegel, “An integrated occupancy and space-use model to predict abundance of imperfectly detected, territorial vertebrates,” *Methods Ecol. Evol.*, vol. 7, no. 5, pp. 508–517, May 2016.

[28] I. Mindru *et al.*, “Copper aluminate spinel by soft chemical routes,” *Ceram. Int.*, vol. 42,

no. 1, pp. 154–164, 2015.

[29] C. Ragupathi, J. J. Vijaya, L. J. Kennedy, and M. Bououdina, “Nanostructured copper aluminate spinels: Synthesis, structural, optical, magnetic, and catalytic properties,” *Mater. Sci. Semicond. Process.*, vol. 24, no. 1, pp. 146–156, 2014.

[30] R. Eason, *Pulsed Laser Deposition of Thin Films*, no. 1. 2007.

[31] R. Jenkins, “X-ray Techniques : Overview,” *Encycl. Anal. Chem.*, pp. 13269–13288, 2000.

[32] K. D. Vernon-Parry, “Scanning electron microscopy: an introduction,” *III-Vs Rev.*, vol. 13, no. 4, pp. 40–44, 2000.

[33] J. I, D. E. Newbury, C. E. Lyman, and D. C. Joy, *Scanning Electron Microscopy and X-Ray Microanalysis*. 1992.

[34] T. S. Tripathi, M. Bala, and K. Asokan, “An experimental setup for the simultaneous measurement of thermoelectric power of two samples from 77 K to 500 K,” *Rev. Sci. Instrum.*, vol. 85, no. 8, 2014.

[35] M. Kracum, A. Kundu, M. P. Harmer, and H. M. Chan, “Novel interpenetrating Cu–Al2O3 structures by controlled reduction of bulk CuAlO2,” *J. Mater. Sci.*, vol. 50, no. 4, pp. 1818–1824, 2015.

[36] J. Ghose and A. Kanungo, “Studies on the thermal decomposition of Cu(NO3)2 · 3 H2O,” *J. Therm. Anal.*, vol. 20, no. 2, pp. 459–462, Apr. 1981.

[37] W. M. Keely and H. W. Maynor, “Thermal Studies of Nickel, Cobalt, Iron and Copper Oxides and Nitrates.,” *J. Chem. Eng. Data*, vol. 8, no. 3, pp. 297–300, Jul. 1963.

[38] M. Aghayan, I. Hussainova, K. Kirakosyan, and M. A. Rodríguez, “The template-assisted wet-combustion synthesis of copper oxide nanoparticles on mesoporous network of alumina nanofibers,” *Mater. Chem. Phys.*, vol. 192, pp. 138–146, 2017.

[39] D. Xiong *et al.*, “Synthesis and Characterization of CuAlO 2 and AgAlO 2 Delafossite Oxides through Low-Temperature Hydrothermal Methods,” *Inorg. Chem.*, vol. 53, no. 8, pp. 4106–4116, Apr. 2014.

[40] C. Ruttanapun *et al.*, “Reinvestigation thermoelectric properties of CuAlO2,” *Energy Procedia*, vol. 56, no. C, pp. 65–71, 2014.

[41] K. Koumoto, H. Koduka, and W.-S. Seo, “Thermoelectric properties of single crystal CuAlO2 with a layered structure,” *J. Mater. Chem.*, vol. 11, pp. 251–252, 2001.

[42] A. T. Burkov *et al.*, “Contribution of spin fluctuations to the low-temperature resistivity and thermopower of YCo2,” *J. Magn. Magn. Mater.*, vol. 177–181, pp. 1069–1070, Jan. 1998.

[43] S. Hébert *et al.*, “Thermoelectric properties of perovskites: Sign change of the Seebeck coefficient and high temperature properties,” *Prog. Solid State Chem.*, vol. 35, no. 2–4 SPEC. ISS., pp. 457–467, 2007.

[44] H. J. Goldsmid, A. R. Sheard, and D. A. Wright, “The performance of bismuth telluride thermojunctions,” *Br. J. Appl. Phys.*, vol. 9, no. 9, pp. 365–370, Sep. 1958.

[45] http://hyperphysics.phy-astr.gsu.edu

9. ACKNOWLEDGEMENTS

Hereby, I express my appreciations to all whom helped me to complete this master’s thesis. I dedicate my sincere gratitude to my supervisors; professor Irina Hussainova and doctor Marina Aghayan for their guidance and support. I could not have imagined having better advisors and mentors for my research. My sincere thank also goes to professor Maarit Karppinen and doctor Tripurari Sharan Tripathi who provided me an opportunity to join their team at Aalto University in Finland as visiting student, and gave me access to the laboratory and research facilities. Without their precious support, it would not be possible to conduct this research. I would like to thank all the researchers and students in the group of Mechanical Engineering at Tallinn University of Technology in the impact hub for their helps during this research.

Last and by no means least, I would like to thank my family; parents, brother, and sister for all the love and support they have given me in my life. My debt to them is beyond measure.